2022

Processing-Microstructure-Property Correlation for 316L Stainless Steel Manufactured by Laser Powder Bed Fusion

Nathalia Diaz Vallejo
University of Central Florida

PROCESSING-MICROSTRUCTURE-PROPERTY CORRELATION FOR 316L STAINLESS STEEL MANUFACTURED BY LASER POWDER BED FUSION

by

NATHALIA DIAZ VALLEJO
MEng. Universidad del Valle, 2017

A dissertation submitted in partial fulfillment of the requirements
for the degree of Doctor of Philosophy
in the Department of Materials Science and Engineering
in the College of Engineering and Computer Science
at the University of Central Florida
Orlando, Florida

Summer Term
2022

Major Professor: Yongho Sohn

ABSTRACT

The microstructural development of 316L stainless steel (316L SS) was investigated over a wide range of systematically varied laser powder bed fusion (LPBF) parameters, such as laser power, laser scan speed, hatch distance, and volumetric energy density. The use of volumetric energy density between 46 and 127 J/mm^3 produced samples with relative density above 99.8% demonstrating that even in the optimized range of processing parameters the pores are unavoidable. Shifting from this range through a variation of laser scan speed produced two types of flaws, lack of fusion (LoF) and keyhole (KH) porosity leading to a decrease in the relative density targeted to higher than 97 %, and about 98 %, and 99 %. The specific mechanism behind the formation of these flaws influences the appearance of the individual pores characterized by circularity, size, and aspect ratio from extensive image analysis of optical micrographs. The samples were tested in uniaxial tension to correlate the flaw characteristics with a yield strength (YS), ultimate tensile strength (UTS), and elongation at failure (EL%). As laser scan speed was increased, the flaw circularity increased in the KH domain while decreased in the LoF domain. The opposite trend was followed by the flaw size and aspect ratio. Additional to the influence of the density, the YS and UTS of the samples showed more sensitivity to the LoF than KH, while the EL% was comparable between the two types of flaws when the porosity is below 2%. The difference in mechanical properties for the 316L SS samples containing KH and LoF flaws with similar density was minimal because of the intrinsically high ductility of the alloy.

In dedication to my family, my partner, and my dog. I am honored to be part of your life. You have made this challenge more bearable with your constant support and encouragement. I will be always here for you.

ACKNOWLEDGMENTS

I would like to express my deepest appreciation to my professor and chair of my committee Dr. Sohn for his invaluable patience and feedback. I am also extremely grateful to my defense committee Dr. Gordon, Dr. Jiang, Dr. Kushima, and Dr. Roy for generously providing knowledge and expertise. Thanks should also go to Fulbright Colombia and ICETEX for providing partial funding for my doctoral studies under the Fulbright Pasaporte a la Ciencia fellowship program.

I would like to recognize my fellow colleagues, especially Dr. Hyer, Dr. Zhou, and Dr. Mehta for their continual mentorship I extend my sincere thanks to Dr. Knezevic and Mr. Kljestan from the University of New Hampshire or their assistance in the mechanical testing, and the staff of the Materials Characterization Facility at UCF for their technical support.

Lastly, many thanks to my family, my partner, his family, Dr. Lopera and Mrs. Peña., without their tremendous understanding and encouragement over the past few years, this endeavor would not have been possible.

TABLE OF CONTENTS

LIST OF FIGURES

LIST OF TABLES

LIST OF ACRONYMS/SYMBOLS

AM	Additive Manufacturing
CAD	Computer Aided Design
EL%	Elongation at Failure
FE-SEM	Field Emission Scanning Electron Microscopy
h	Hatch Distance
HIP	Hot Isostatic Pressing
KH	Keyhole Porosity
LoF	Lack of Fusion Porosity
LPBF	Laser Powder Bed Fusion
P	Laser Power
v	Laser Scan Speed
d	Melt Pool Depth
OM	Optical Microscopy
PBF	Powder Bed Fusion
t	Powder Layer Slice Thickness
SS	Stainless steel

SLM	Selective Laser Melting
UTS	Ultimate Tensile Strength
VED	Volumetric Energy Density
XRD	X-Ray Diffraction
YS	Yield Strength

CHAPTER 1: INTRODUCTION

With the ability to build material through successive adding of layers, laser powder bed fusion (LPBF) is a promising technology with a high degree of design freedom particularly useful for very complex shapes that are often impossible or very challenging to produce by subtractive manufacturing methods. Other advantages include easy quality control through the incorporation of health monitoring sensors, and high material efficiency with reduction of waste production [1], [2]. Figure 1 graphically shows the main components inside an LPBF machine.

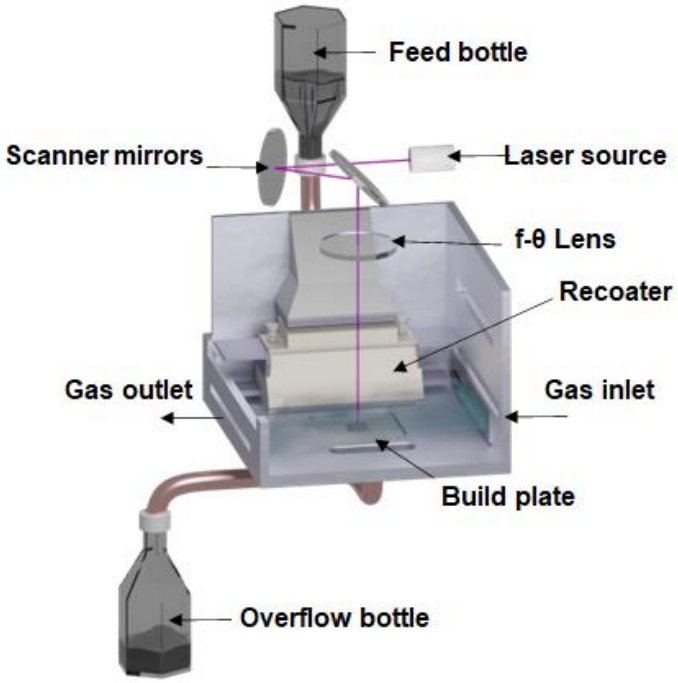

Figure 1: Schematic of LPBF system with the main components

Several processing parameters commonly classified as [3]: (1) laser-related parameters, (2) scan-related parameters, (3) powder related parameters, and (4) build environment parameters, influence the densification mechanism and microstructural features of materials processed by the LPBF technology. The optimization of these processing parameters to produce defect-free, fully dense components is one of the challenges for LPBF. Although considerable research effort has focused to address this requirement, the components made by means of this method still contain some number of flaws that can compromised mechanical properties.

1.1 Motivation

The presence of flaws in an LPBF component, caused by the laser beam and powder interactions during the process, can play a significant role in failure. Previous studies have been focused on understanding and suppressing flaw formation [4]–[7] mainly by processing parameter optimization. Despite these efforts, the flaws are unavoidable, limiting the application of LPBF technology and resulting in high part rejection and/or avoidance of the technology.

Therefore, it is important to determine which type of process-induced flaw, categorized as keyhole (KH) or lack of fusion (LoF), can be tolerated over the other starting with the exploration of the effect of the process parameters on LPBF porosity follow by a statistical

analysis of the individual flaw's characteristics (size, frequency, morphology, and distribution) and the correlation with the tensile properties.

1.2 Objectives

In this dissertation, the correlation between part density and processing parameters of 316L stainless steel fabricated by laser powder bed fusion (LPBF) was investigated. To that end processing parameters were independently varied as a function of laser power, laser scan speed, and hatch distance to produce different mechanisms in porosity/flaw formation. Solidification microstructure development from laser-material interaction was documented at function of LPBF parameters. Based on the results of the optimization study, it was possible to determine the volumetric energy density domain for a given type of flaw and generate similar density levels by intentionally introducing internal porosity. Finally, the influence on the mechanical properties of process-induced flaws was studied.

CHAPTER 2: LITERATURE REVIEW

2.1 Background on Additive Manufacturing

Additive manufacturing (AM), commonly known as three-dimensional (3D) printing, is an emerging technology initially proposed for producing prototypes but nowadays employed for building functional and structural components with complex geometry from a 3D model data [1], [2]. AM technologies are generally categorized into seven categories based on the basic principle of binding [8]: (1) binder jetting, (2) directed energy deposition (DED), (3) material extrusion, (4) material jetting, (5) sheet lamination, (6) vat polymerization and (7) powder bed fusion (PBF).

Among the PBF techniques, Laser Powder Bed Fusion (LPBF), also known as Selective Laser Melting (SLM), is very promising in preparing the metallic materials and, therefore, have been well-researched in both industry and academia. Several commercial alloys have been successfully used to manufacture engineering components by LPBF, including those based on titanium [9]–[11], iron [12][13], aluminum [14]–[16], and nickel-based superalloys [17]–[19].

The build-up process for LPBF, involves heating, melting, and solidification of a deposited thin layer of metallic powder by a raster motion of the laser heat source using

galvanometer driven mirrors. Once a layer has been completed, the build plate is lowered, a new layer of powder is spread over the previous layer(s), and the loading/powder addition process is repeated until the component is finished [3].

In LPBF the processing parameters are commonly classified as [3]: (1) laser-related parameters (e.g., laser power, spot size, pulse duration, and pulse frequency), (2) scan-related parameters (e.g., scan speed, hatch distance, scan rotation, and scan pattern), (3) powder-related parameters (e.g., powder morphology, particle size and distribution, layer thickness, dosing, and materials properties), and (4) build environment parameters (e.g., powder bed temperature and its uniformity, gas flow, gas type, spreader bar type).

Because of the high number of processing parameters, an index known as the volumetric energy density (VED) is used to summarize the energy level per unit volume considered during layer melting, as represented in Figure 2. VED is defined in Equation (1) by the ratio of laser power (P) supplies to the product of laser scan speed (s) with hatch distance (h) and layer thickness (t) [20].

$$\text{Volumetric energy density (VED)} = \frac{P}{v \cdot h \cdot t} \qquad (1)$$

In general, there is an optimal combination of these processing parameters, i.e., a process window in which the process-induced porosity is minimized.

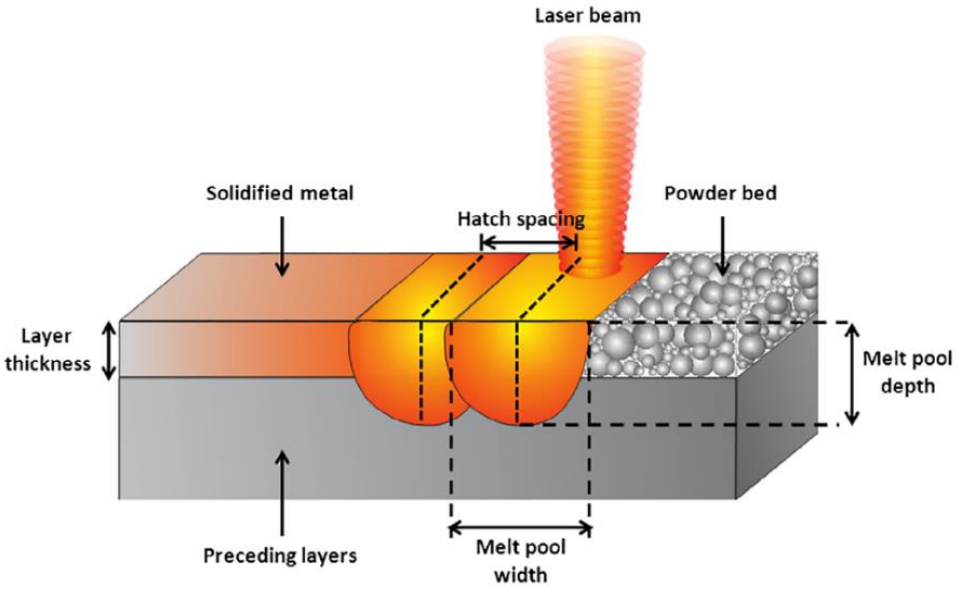

Figure 2: Schematic of LPBF processing parameters [21]

2.2 LPBF of 316L Stainless Steel

The grade 316L (316L SS) belongs to the 300 series of austenitic stainless steels and is one of the most widely investigated materials for LPBF. Its carbon content lower than 0.03 wt. % confers it good weldability. Its excellent corrosion resistance is attributed to the formation of a stable passive chromium- rich oxide film on the surface due to the presence of chromium (Cr > 16 wt. %). Additional to the good weldability and excellent corrosion resistance, its good mechanical properties make it of interest to numerous applications including marine [22], biomedical equipment [23] and fuel cells [24].

Several studies have reported on the densification in LPBF 316L SS by means of the improvement of the quality in the feedstock materials, optimization of the processing parameters, optimization of scanning and building strategies and alternatively post-processing heat treatments to counter this effect [4]–[7]. Li et al.[4] found that the process to produce powders influence the density of the part. Gas-atomized powder had lower oxygen content, a spherical shape, and smaller mean particle size than water atomized powder and thereby possessed higher packing density and powder flowability which was in favor of LPBF densification. Choi et al., [5] reported an optimal volumetric energy density range 58–200 J/mm^3 for LPBF 316L SS, with which nearly fully dense samples (above 98.5% of the theoretical density) were obtained. Larimian et al. [6] studied the effect of the scanning strategy concluding that the use of alternate hatches and a single pass of a laser beam along with a volumetric energy density of 150 J/mm^3 resulted in the highest densification (relative density of 99.45 %) as well as improved mechanical properties. Chadha et al. [7] observed a relative density of 99.9% after a combination of hot isostatic pressing (HIP) at 1163 °C for 3 h at a pressure of ~1 Mbar and annealing at 900 °C for 2 h followed by nitrogen quenching at 5–6 bar until 65 °C. The authors explained this result as the consequence of the applied pressure during HIP that allows the material to flow and sinter at elevated temperatures.

2.3. Understanding Solidification of LPBF Processing

Melt pool geometry is fundamentally determined by the total amount of input energy which is absorbed by the powder bed as the laser beam scans. Melt pool features are indicators of the heat transfer, solidification behavior, and defects formation. From welding literature [25], two different melting modes can be distinguished depending on the resultant melt pool characteristics:

(1) Conduction mode: Occurs when a relatively low laser energy intensity is used. The laser energy is absorbed mainly by the upper layers of the part, no vaporization occurs, and heat transfer takes place primarily through conduction and convection in the melt pool. Conduction mode generally produces semicircular melt pools or melt pools with small aspect ratios (depth/width), as illustrated in Figure. 3 (a). Tenbrock et al, [26] defined a threshold for the conduction mode as a melt pool with an aspect ratio below 0.8.

(2) Keyhole mode: Occurs when the laser energy intensity is sufficient to cause a significant vaporization of material on the surface, so the vaporized material produces a recoil momentum pressure which pushes down the molten metal resulting in the formation of a vapor depression cavity, i.e., the keyhole, that enhances the laser absorption due to multiple reflections of the laser beam along the keyhole walls [27]. This enables the laser beam to “drill” to a far deeper depth than is possible in conduction mode, as shown in Figure 3 (b). The keyhole mode is considered an unstable process and the keyhole

collapse often results in the formation of a bubble in the melt pool. If the bubble fails to escape from the melt pool, porosity is formed [28].

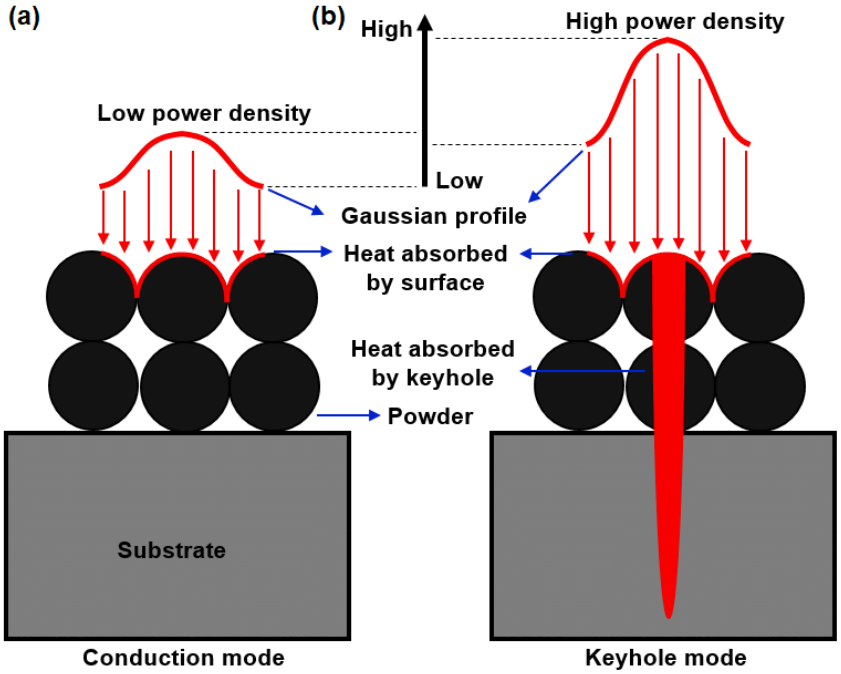

Figure 3: Schematic of laser energy absorption in (a) the conduction mode and (b) the keyhole at the initial moment. The laser assumed to have a Gaussian distribution [28]

The microstructure of the as-built LPBF 316L SS has been reported as highly heterogeneous with fusion boundaries, dendritic and cellular walls, dislocations, precipitates, segregated elements (for example, Cr and Mo), and atomic scale impurities (for example, N and H) [29]–[32]. Wang et al. [29] reported an empirical relationship between yield strength and subgrain cell size (λ) as, $\sigma_y = 183.31 + \left(253.66/\sqrt{\lambda}\right)$, based on the assumption of Hall–Petch-type strengthening behavior.

2.4. Flaws in LPBF

Despite the significant progress in producing a nearly fully dense material [4]–[7], flaws[1] seem to be unavoidable and have been reported to form in LPBF parts even at the optimal processing conditions. The most commonly found processing-related flaws in LPBF components are lack-of-fusion (LoF) and keyhole (KH) porosity [33]. As shown in Figure 4, there is a general relationship between these flaws and the processing parameters, which states that LoF pores develop when there is insufficient input energy applied to the metal powder bed, (e.g., low power or high speed), leading to a small melt pool and incomplete melting, i.e., residual interparticle space. Conversely, under high energy input (e.g., high power or slow speed), significant vaporization leads to KH formation [34].

[1] For clarity throughout the dissertation, we employ the term “flaw” in describing both the lack-of-fusion “pores” and keyhole “pores.”

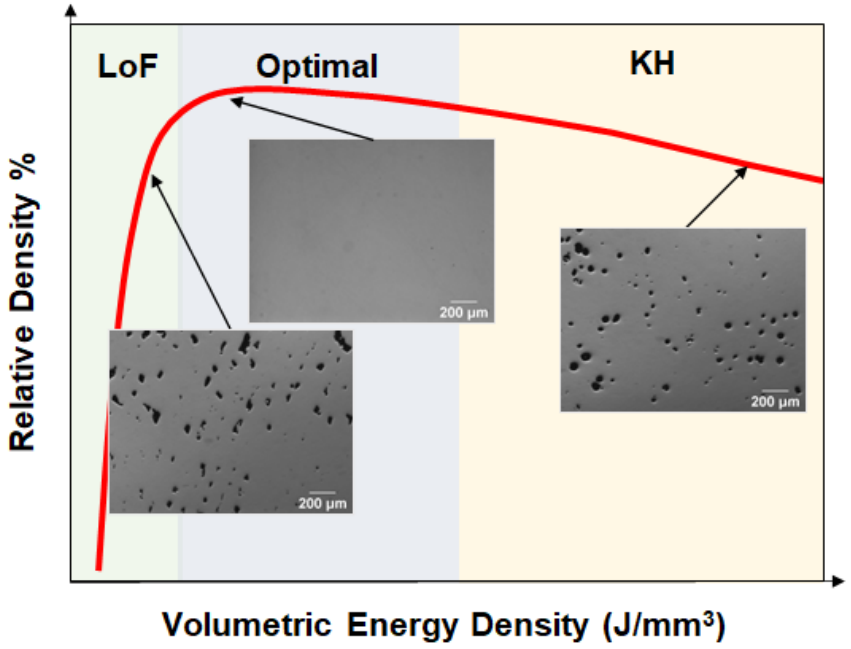

Figure 4: General relationship flaws-processing parameters

For a deposited layer to bond properly with a previous layer, the melt pool depth, d, should exceed the layer thickness, t, and adequately remelt the previously deposited layer. Mukherjee et al.[35] proposed a non-dimensional lack of fusion index (LF), defined by the Equation 2, to examine adequate fusion and inter-layer bonding for different alloys:

$$LF = \frac{d}{t} \qquad (2)$$

When the index is larger than a threshold, LoF pores may form inside the sample. By plotting the LF against the linear heat input (P/v), it was shown that for a given heat

input, 316 SS will have the lowest value of LF. Therefore, 316 SS is most susceptible to LoF porosity, among the alloys considered, as shown in Figure 5

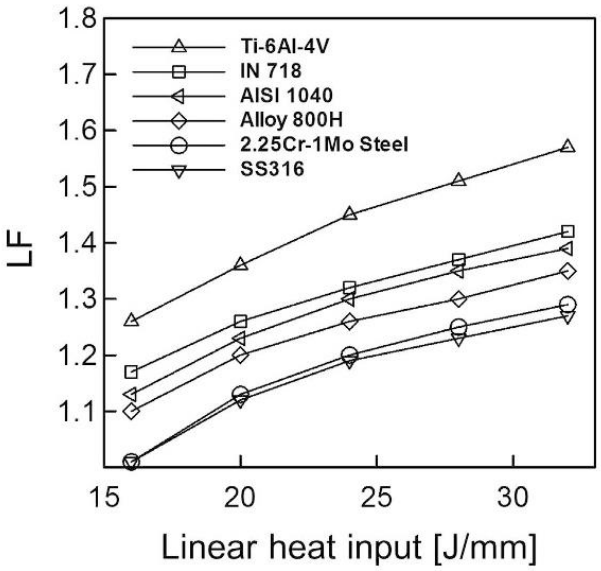

Figure 5: Correlation between LF and linear heat input for Ti6Al4V, IN 718, AISI 1040, Alloy 800H, 2.25Cr-1Mo Steel and 316L SS [35]

Tang et al. [36] formulated a relationship between the occurrence of LoF and the melt pool dimensions, accounting for the influence of the hatch distance, h, and the melt pool width, w, and expressed by the Equation 3 as follows:

$$\left(\frac{h}{w}\right)^2 + \left(\frac{t}{d}\right)^2 \leq 1 \qquad (3)$$

In the case where the criterion is more than 1, incomplete melting occurs, and the lack of fusion porosity is predicted. For the case less than 1, lack of fusion porosity is avoided due to overlapping melting.

Unlike the LoF pores induced by the LPBF processing conditions, when the spatter particles form and land onto the powder bed, where the laser has yet to pass, can shield powder below from the laser energy also resulting in a lack of fusion porosity [37]. Appropriate powder sieving techniques, and effective gas flow can prevent powder-induced lack of fusion porosity.

Due to re-melting while depositing the next layer, there is a possibility for gas bubbles created on top of the melt pool to scape as opposed to the gas bubbles deeper in the melt pool which makes them more detrimental.

Because of the different formation mechanisms, these pores often exhibit distinct physical and microstructural characteristics [38]. LoF pores can manifest as irregular pores with sharper edges and flattened shape and can contain entrapped un-melted particles. On the other hand, the KH pores are typically characterized as nearly spherical in shape.

To simplify the complexity of the process-induced flaws, intentionally introduced features through computer aided design (CAD) have been used to precisely control flaw size, spacing, and distribution towards evaluating the porosity threat [39]–[41]. For

example, Wilson-Heid et al. [39] created an artificial penny-shaped void at the center of the LPBF 316L SS cylindrical tensile samples within 6.0 mm gauge diameter, varying void diameters from 150 μm to 4800 μm. The penny-shaped voids with a diameter larger than 2400 μm (16% of the cross-section area) reduced UTS, while the elongation to failure was significantly affected by the penny-shaped voids with a diameter larger than 1800 μm (9% of the cross-sectional sample area).

Similarly, Meng et al. [40] analyzed the effect of the diameter (100 μm, 300 μm, 500 μm, and 1000 μm) as well as location (center, sub-surface, near-surface) of built-in spherical voids in LPBF Ti-6Al-4V. It was found that spherical pores with diameters 500 μm (0.7% of the cross-sectional area) and smaller had negligible influence on the elastic modulus and tensile strength, but that the elongation at failure was reduced with voids of 1000 μm in diameter (2.8% of the cross-sectional area). Moreover, the elongation to failure decreased as the embedded pore became closer to free surface.

Unlike Wilson-Heid et al. [39] and Meng et al.[40], Kim et al. [41] embedded a more complex internal geometry of internal void (octahedron-shaped) in the gauge length of the 17-4 SS tensile samples.

Since the minimum flaw size that can be formed by CAD is limited by the geometrical resolution of the LPBF system, the artificially designed flaw would not be fully representative of either the KH or the LoF. Additionally, the use of this methodology omits the physics associated with inherent flaws from LPBF [42].

Other studies have modified the LPBF processing parameters to introduce the process-induced flaws [11]. Montalbano et al. [11] studied LPBF Ti-6Al-4V samples with similar amounts of flaw, and reported that samples with predominately LoF pores tend to have lower strength, as compared to samples containing KH pores. Moreover, the elongation at failure was substantially lowered in both cases as the flaw amount increased.

Carlton et al, [43] studied LPBF 316L SS samples built with 100 W power, and speeds of 222 mm/s and 400 mm/s for the low and high porosity groups, respectively. The high porosity sample (overall average porosity >2.2%) with large inhomogeneous void distributions (with regions within the specimen where porosity reaches 17%), and flaws highly irregular and with pointed features, displayed flaw-driven failure, with cracks initiated at pre-existing voids. The UTS for samples with high porosity was determined as 540 ± 120 MPa compared with 630 ± 60 determined for low porosity samples (Estimated porosity 0.17±0.04%).

CHAPTER 3: METHODOLOGY

3.1. Powder Characterization

The starting material used in this study was gas atomized 316L SS powders acquired from SLM Solutions (SLM Solutions Group AG, Lübeck, Germany). The powder size distribution was determined using a Beckman-Coulter (Beckman Coulter, Inc., Brea, CA, USA) LS 13 320 laser diffraction particle size analyzer. Powder morphology and cross-sections were examined with the field emission scanning electron microscopy (FE-SEM) Zeiss Ultra-55 (Carl Zeiss AG, Jena, Germany), equipped with an X-ray energy dispersive spectroscopy (XEDS) operating at an accelerating voltage of 20 kV. Standardless semi-quantitative analyses from XEDS data were carried out using Noran System 7 Version 3.0 software (Thermo Fisher Scientific Inc., Madison, WI, USA) for the estimation of compositions.

Phase determination for the powders was performed by X-ray diffraction (XRD) using an PANalytical Empyrean (Worcestershire, UK), which uses the Bragg-Brentano diffraction focusing geometry.

To study powder morphology and cross-section, powder was cold mounted in epoxy. After curing, the epoxy puck was polished with SiC and diamond paste, with a final finish of 0.05 μm with colloidal silica.

3.2 LPBF Processing

3.2.1 The SLM 125HL LPBF System

For all LPBF processing, a SLM 125HL (SLM Solutions Group AG, Lubeck, Germany), shown in Figure 6(a), was employed. The SLM 125HL is equipped with a single ytterbium fiber laser (IPG Photonics, Oxford, MA, USA) with laser power up to 400 W, a continuous wavelength of 1070 nm, and a beam focus diameter of about 70 μm. Preheating of the build plate was set at 100 °C and Argon was used to maintain the inert atmosphere by keeping the O_2 content below 0.1% during LPBF.

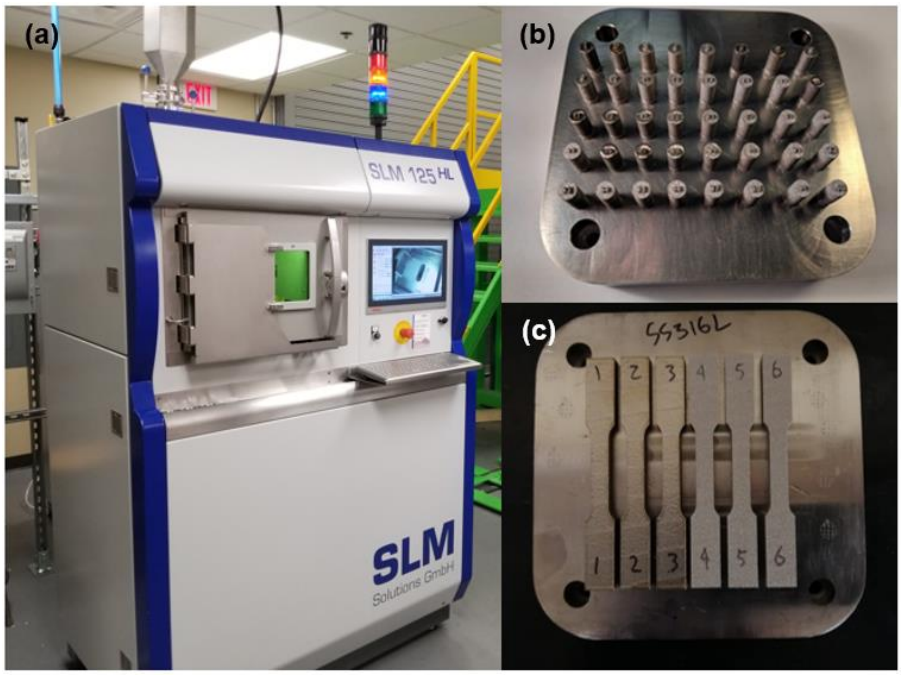

Figure 6: (a) LPBF system used for all experiments and (b) photos of the 316L SS cylindrical and (c) tensile test specimens

3.2.2 Parametric Investigation and LPBF Process

To study the effects of LPBF processing parameters on densification, cylindrical samples (12 mm in height and 6 mm in diameter) were built with the SLM 125HL, as shown in Figure 6(b). Build direction was parallel to the height of the cylindrical samples. The cylinders were built 4 mm above the build plate, supported underneath with a typical block support structure that consisted of 0.2 mm thick walls separated every 0.8 mm.

The processing parameters, laser power, scan speed and hatch spacing, were varied independently with due consideration for normalized volumetric energy density (Equation (1)), as listed in Table 1. The following conditions were held constant throughout this study: 0.03 mm layer thickness, 10 mm stripe width, 0.08 mm stripe overlap, 67° scanning rotation between subsequent layers and a stripe scanning strategy. The bordering, contouring, as well as up-skin, and down-skin parameters were all deactivated to reduce the effects of other processing conditions as well as the preserve the last layer melted on the top of the parts.

Table 1: Laser powder bed fusion parameters examined for 316L SS

Series	Power (W)	Scan speed (mm/s)	Slice thickness (mm)	Hatch distance (mm)	Energy density (J/mm^3)	Relative density (%) measured by image analysis
I	125	100	0.03	0.12	347.2	96.35 ± 0.79
		200			173.6	96.79 ± 1.35
		400			86.8	99.09 ± 0.28
		600			57.9	99.90 ± 0.08
		800			43.4	99.51 ± 0.30
	200	200			277.8	98.35 ± 0.53
		400			138.9	99.49 ± 0.27
		600			92.6	99.92 ± 0.05
		800			69.4	99.89 ± 0.06
		1000			55.6	99.88 ± 0.07
		1200			46.3	99.83 ± 0.05
		1400			39.7	99.44 ± 0.20
		1800			30.9	96.60 ± 1.74
		2200			25.3	94.23 ± 1.00
		2600			21.4	90.22 ± 3.17
	275	400			191.0	98.74 ± 0.64
		600			127.3	99.9 ± 0.07
		800			95.5	99.91 ± 0.14
		1000			76.4	99.98 ± 0.01
		1200			63.7	99.77 ± 0.10
		1400			54.6	99.87 ± 0.06
		1800			42.4	99.62 ± 0.14
		2200			34.7	99.09 ± 0.41
		2600			29.4	96.55 ± 0.59
		3000			25.5	93.52 ± 1.62
	350	600			162.0	99.74 ± 0.08
		800			121.5	99.93 ± 0.05
		1000			97.2	99.90 ± 0.03
		1200			81.0	99.98 ± 0.02
		1400			69.4	99.78 ± 0.23
		1800			54.0	99.71 ± 0.18
		2200			44.1	99.46 ± 0.32
		2600			37.4	95.09 ± 2.00
		3000			32.4	94.40 ± 1.47
		3400			28.6	94.90 ± 1.32

Series	Power (W)	Scan speed (mm/s)	Slice thickness (mm)	Hatch distance (mm)	Energy density (J/mm^3)	Relative density (%) measured by image analysis
II	200	800	0.03	0.08	104.2	99.98 ± 0.03
				0.1	83.3	99.99 ± 0.01
				0.12	69.4	99.97 ± 0.02
				0.14	59.5	99.91 ± 0.04
				0.16	52.1	99.84 ± 0.07

Based on the results of the parametric investigation, the laser scanning speed was varied to target three levels of density (i.e., > 97 %, ~ 98 % and ~ 99 %) in the KH and LoF domains and near fully dense (i.e., 99.9 %) specimens as listed in Table 2. With these parameters, traditional dog-bone specimens with a gauge length of 25 mm in accordance with tolerances described in ASTM E8/E8M were manufactured in a vertical build direction with three repetitions per set of LPBF parameters, as shown in Figure 6(c). The samples were then removed from the built plate by wire electrical discharge machining and the top/bottom surfaces and edges were polished down to 1200 grit with SiC grinding paper to generate consistent sample surface.

Table 2: LPBF processing parameters used to produce samples of varying flaw type at three levels of density, and the corresponding mechanical properties.

Power (W)	200						
Hatch Distance (mm)	0.12						
Slice Thickness (mm)	0.03						
Scan Speed (mm/s)	200	400	500	800	1200	1500	1700
Volumetric Energy Density (J/mm^3)	277.8	138.9	111.1	69.4	46.3	37.0	32.7
Density XZ (%)	96.9 ± 2.7	97.6 ± 0.4	99.6 ± 0.1	99.9 ± 0.1	98.9 ± 0.2	96.7 ± 0.7	90.0 ± 1.5
Density XY (%)	96.9 ± 2.3	97.8 ± 0.7	99.6 ± 0.1	99.9 ± 0.1	99.2 ± 0.2	96.6 ± 0.5	91.2 ± 2.2
Flaw Type Identified	Keyhole			Negligible	Lack of Fusion		

Yield Strength (MPa)	502.7 ± 10.1	567.3 ± 1.2	583.3 ± 0.4	565.7 ± 7.7	550.4 ± 0.5	511.3 ± 9.6	415.6 ± 5.0
Tensile Strength (MPa)	597.1 ± 16.8	669.9 ± 0.7	686.3.1 ± 2.2	672.9 ± 3.9	665.4 ± 2.3	634.5 ± 9.3	510.9 ± 11.9
Elongation at Failure (%)	18.8 ± 3.1	39.8 ± 2.3	40.6 ± 0.6	41.9 ± 0.9	43.3 ± 1.6	38.9 ± 1.6	13.1 ± 2.6

3.3. Microstructural and Phase Analysis

Each cylindrical sample and six grip sections of the tensile bars (one for each set of processing parameters), were cross-sectioned both parallel and perpendicular to the build direction, referencing these cuts as the XZ and XY planes respectively, as shown in Figure 7.

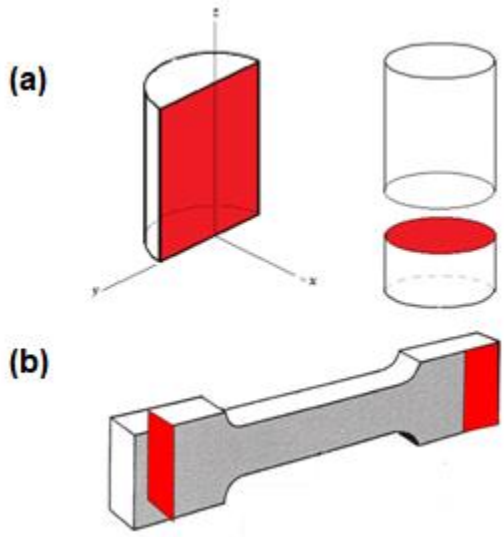

Figure 7: Vertical (XZ) and horizontal (XY) cross-sections of the (a) cylindrical and (b) tensile bars specimens (not to scale)

The cross-sections were cold mounted in epoxy. and metallographically prepared with SiC grinding papers and diamond paste polishing, with a final finish of 0.05 mm using colloidal silica.

Following, five optical metallographs for the cylindrical samples and fifteen for the grip sections of the tensile bars were taken at 100 X and 50 X magnification using the Nikon Metaphot microscope (Nikon Metrology Inc, Tokyo, Japan) for flaw quantification. The cross sections of the cylindrical samples were then etched by immersion for approximately 40 to 60 s in the mixed acids reagent consisting of hydrochloric acid: acetic acid: nitric acid in 3:2:1 volume ratio for detailed microstructural analyses.

ImageJ [44] (National Institute of Health, Bethesda, MD, USA) was employed to quantitatively determine:

(1) Density: The images were edited with the image post-processor ImageJ and were then separated into dense areas and flaws. Afterward, the ImageJ tool “Analyze Particles” was executed. This Plug-In analyzes objects in binary or images after thresholding. By scanning the image, it outlines objects and measures them, then resumes the scanning procedure until it reaches the end of the image or selection. The total area of flaws was subtracted from 100 % to obtain the part relative density.

(2) Size: Maximum Feret diameter, i.e., the longest distance between any two points along the pore boundary was determined to quantify the size.

(3) Shape: Shape descriptors such as aspect ratio and circularity were determined to describe geometric characteristics of the flaws. The aspect ratio of the flaws was the

measure of elongation defined by the ratio between maximum and minimum Feret diameter. The circularity was quantified by using the Equation 4:

$$\text{Circularity} = \frac{4\pi(\text{Area})}{(\text{Perimeter})^2} \quad (4)$$

For a given sample, the amount of porosity/flaw observed did not vary significantly between the cross-sectional planes in build direction and the normal, so only the results from the cross-section parallel to the build direction were reported and analyzed.

(4) Melt pool geometry: The initial layer of the build was set such that cross-sectional microscopy would allow for the measurement of melt pool width and depth using the final, top LPBF layer, without any repeated laser melting or thermo-cycling. With the assumption of symmetry within each melt pool, the melt pool width was measured from the edge to the center and multiplied by a factor of 2 to obtain the approximated width value.

3.4. Mechanical properties determination

To assess the mechanical behavior of as-built LPBF 316L SS, room temperature uniaxial tensile tests were conducted quasi-statically using an MTS Landmark 370 (MTS Systems Corporation, Eden Prairie, MN USA). The loading system is equipped with a 250 kN load cell. A quasi-static strain rate of 1×10^{-3}/s was employed. Three tests per set of

processing parameters were carried out at the University of New Hampshire, Durham, NH, USA using a static axial clip-on extensometer attached to the gage section of the specimen.

Fracture surface details (e.g., flaws) and mode of fracture were characterized with the field emission scanning electron microscopy (FE-SEM) Zeiss Ultra-55 (Carl Zeiss AG, Jena, Germany),

CHAPTER 4: PROCESS OPTIMIZATION AND MICROSTRUCTURE ANALYSIS TO UNDERSTAND LASER POWDER BED FUSION OF 316L STAINLESS STEEL

A percentage of the work contained in this chapter was published in N. D. Vallejo, C. Lucas, N. Ayers, K. Graydon, H. Hyer, and Y. Sohn, “Process optimization and microstructure analysis to understand laser powder bed fusion of 316l stainless steel,” *Metals* (Basel)., vol. 11, no. 5, 2021. [45]

4.1. Starting 316L Stainless Steel Powders

The gas-atomized 316L SS powders were spherical in shape with occasional satellites as presented in Figure 8a. The cross-sectional backscatter electron micrograph shown in Figure 8b clearly revealed the rapidly solidified dendritic microstructure. The particle size in Figure 8c exhibited a Gaussian-type distribution. The measured D10, D50 and D90 values were, respectively, 22.0 µm, 35.5 µm and 50.0 µm. XRD pattern in Figure 8d confirmed the presence of the FCC austenite phase, without any detectable presence of the ferrite phase. The powder composition from the SEM-XEDS measurement is reported in Table 3 and is close to the specification published by SLM. (Solutions Group AG, Lübeck, Germany).

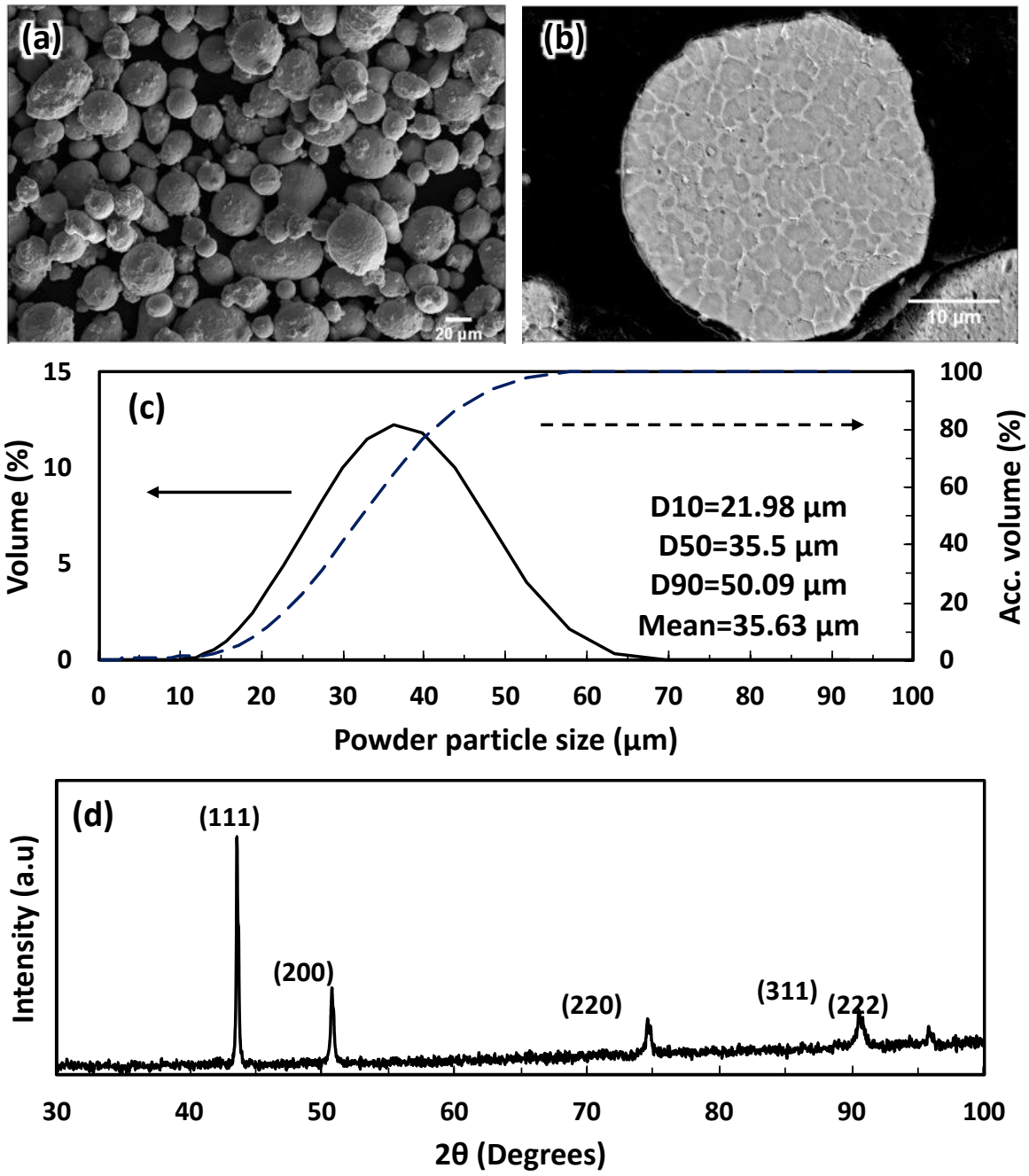

Figure 8**:** Characteristics of the gas atomized 316L SS powders examined by (a) secondary electron micrograph; (b) cross-sectional backscatter electron micrograph; (c) powder size distribution; and (d) X-ray diffraction pattern

Table 3: Chemical composition of the gas atomized 316L SS powders determined by SEM-XEDS and the nominal composition specification from SLM Solutions Group AG (SLM Solutions Group AG, Lübeck, Germany)

	Si	Cr	Mn	Fe	Ni	Mo
SEM-XEDS	0.7 ± 0.1	18.5 ± 0.2	1.8 ± 0.2	68.3 ± 0.3	8.9 ± 0.1	1.8 ± 0.1
SLM Specification	max 1.0	16.0 - 18.0	max 2.0	BAL.	10.0 - 14.0	2.0 - 3.0

4.2. Influence of L-PBF Parameters on the Density

Figure 9 presents representative optical micrographs of samples examined (series I in Table 1) and quantified using image analysis. Dark contrast features correspond to pores and flaws in the as built 316L SS. The dotted region in Figure 9 with energy density values between 45 and 125 J/mm^3 produced samples with density greater than 99.8% determined by image analysis.

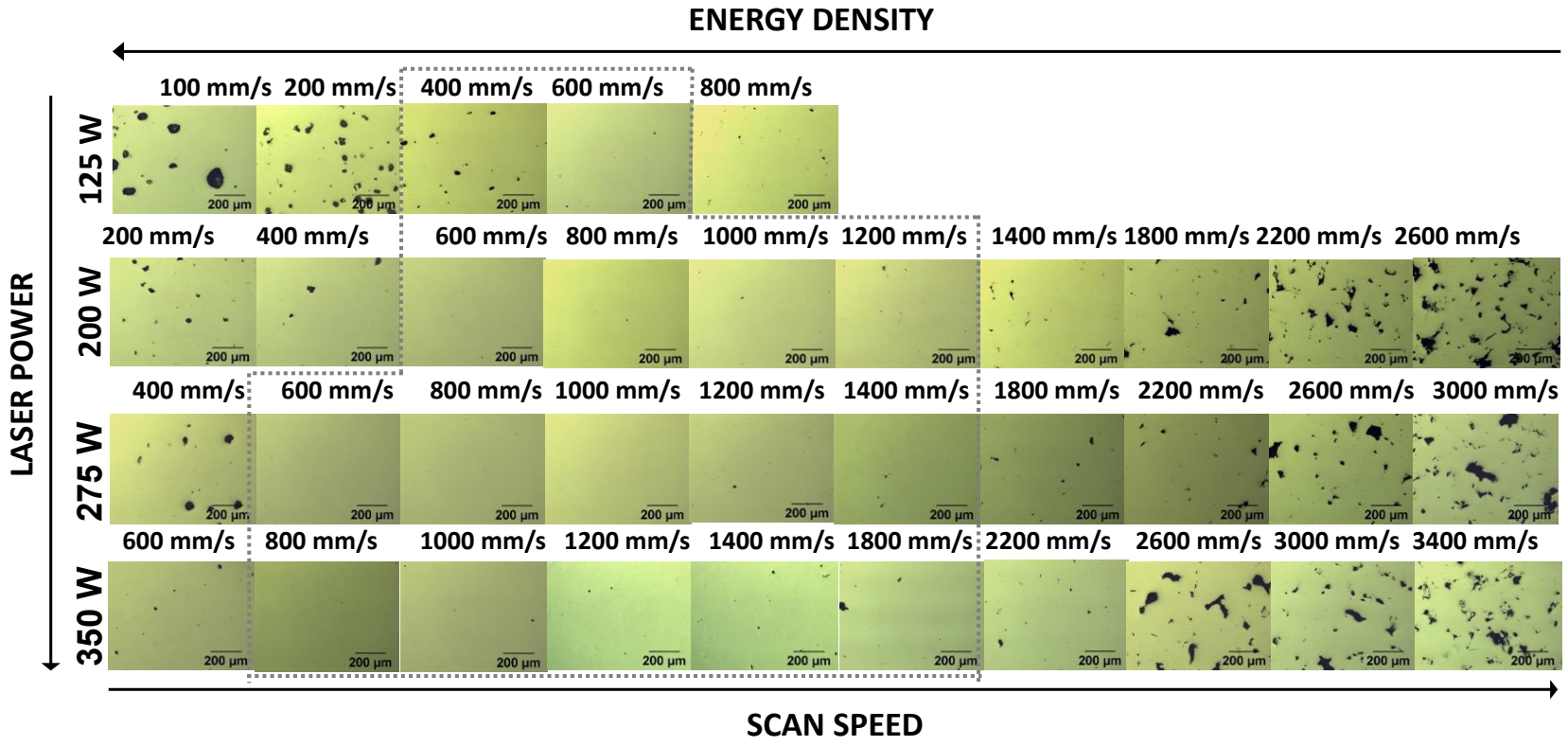

Figure 9: Optical micrographs from the cross-sections parallel to the build direction for LPBF 316L SS (Serie I) built as functions of laser power and scan speeds. Hatch distance and slice thickness were kept constant at 0.12 mm and 0.03 mm, respectively

Lower volumetric energy density, for example, with high laser scan speed at a constant laser power yielded more irregular-shaped flaws due to insufficient melting, i.e., lack of fusion flaws. Higher energy density on the other hand produced more rounded pores, which can be attributed to the keyhole effect. The presence of flaws and/or pores decreased significantly for a range of intermediate volumetric energy density. To quantify these observations, an extensive image analysis was carried out.

Figure 10(a) presents the relative density determined from samples produced by LPBF as function of scan speed for various laser power employed as listed in Table 1 (series I). In general, relative density increased sharply with an increase in scan speed, remained above 99.8%, then decreased gradually with a further increase in scan speed. Density higher than 99.8% was observed for the sample produced with the scan speed from 600 mm/s to 1200 mm/s, from 600 mm/s to 1400 mm/s, and from 800 mm/s to 1400 mm/s for the laser power of 200 W, 275 W and 350 W, respectively.

The same results from density measurement can be presented as a function of volumetric energy density, as plotted in Figure 10(b). The density of the samples sharply increased from ~90% with an increase in volumetric energy density and reached a density greater than 99.8% around 46 J/mm^3. The density remained greater than 99.8% from 46 J/mm^3 to 127 J/mm^3 but decreased gradually down to ~95% with a further increase in volumetric energy density, as presented in Figure 10(b). Within the LPBF parameters examined in this study, using constant hatch spacing and slice thickness of 0.12 mm and

0.03 mm, respectively, the density variation could be described well by the volumetric energy density variation.

Figure 10(c) presents the circularity of the flaws as a function of scan speed for a laser power of 200 W. Circular pores with circularity near 1 would more likely correspond to keyhole pores, while circularity much lower than 1 would correspond to flaws originating from insufficient melting, i.e., lack of fusion flaws from interparticle space residuals. At very low scan speeds, where keyhole pores may develop, flaws with slightly lower circularity were observed, perhaps due to an incomplete coalescence of multiple keyhole pores. At very high scan speeds, where lack of fusion flaws may develop, flaws with lower circularity were observed. Between 600 mm/s and 1000 mm/s of scan speed, circularity higher than 0.9 was observed for the laser power of 200 W employed. This trend in circularity was similar for other laser powers employed. The LPBF parameter specified by SLM Solutions, (power = 200 W; scan speed = 800 mm/s; hatch spacing = 0.12 mm; slice thickness = 0.03; energy density = 69.4 J/mm^3) corresponded to the very high density (>99.8%) and very high circularity (>0.95). Therefore, this corresponds to the optimum LPBF parameter set determined in this study.

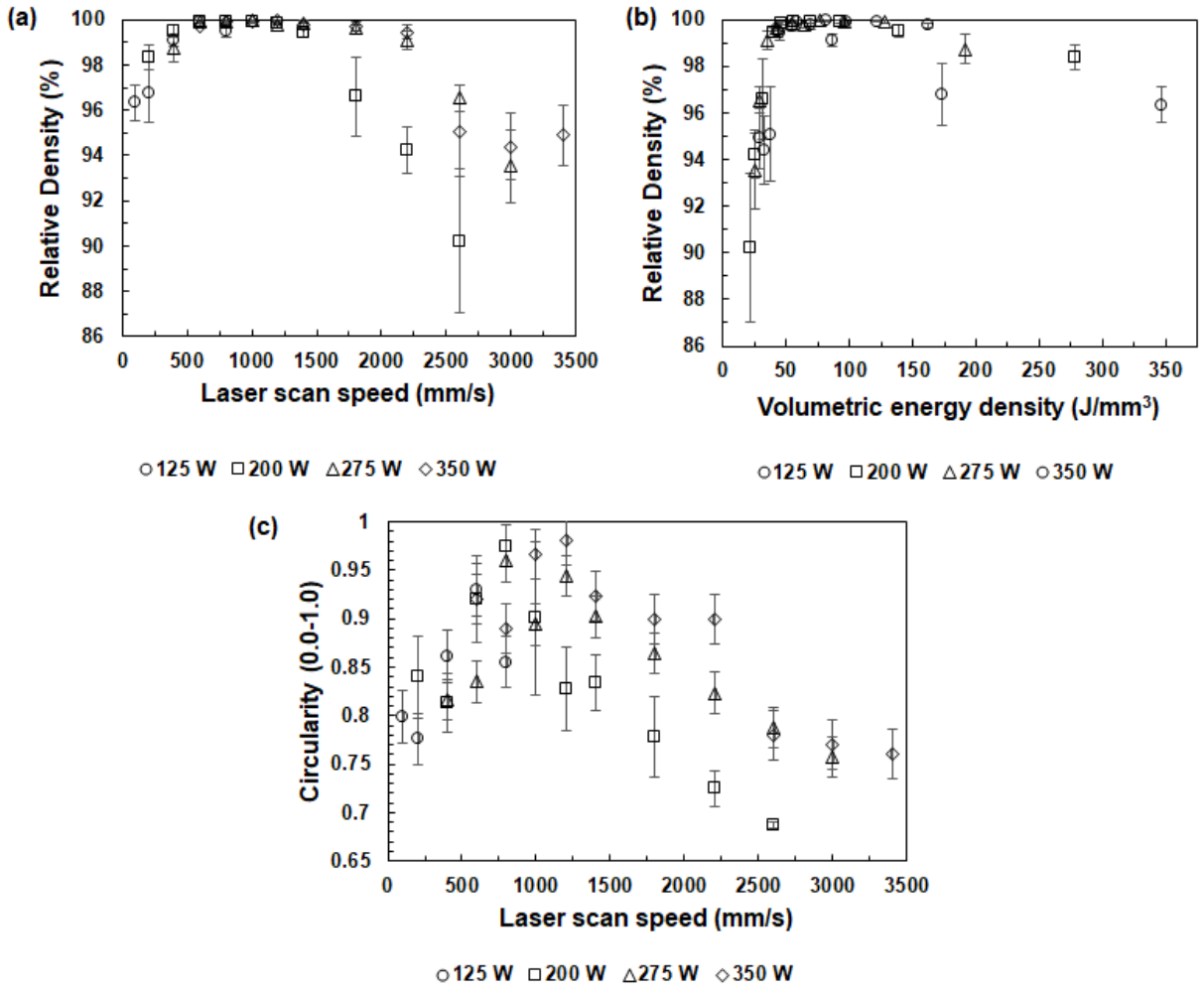

Figure 10: Relative density as a function of (a) laser scan speed and (b) volumetric energy density; (c) Circularity of flaws as a function of laser scan speed with hatch distance, and slice thickness held constant at 0.12 mm, and 0.03 mm, respectively

To examine the effect of hatch distance, LPBF of 316L SS was carried out using 0.08 mm, 0.1 mm, 0.12 mm, 0.14 mm and 0.16 mm, while the laser power, scan speed, and slice thickness were held constant at 200 W, 800 mm/s, and 0.03 mm, respectively. This investigation corresponds to series II in Table 1. In general, as the hatch distance

decreased, the density increased, as presented in Figure 11(a), although the relative density remained mostly greater than 99.8%. This would be attributed to the fact that even at the large hatch distance of 0.16 mm, which is much larger than the powder size or laser beam diameter, the melt pools are sufficiently large, and they overlap to minimize the lack of fusion flaws. Still, with an increase in hatch distance, the circularity of the pores decreased, as demonstrated in Figure 11(b), which indicates the progressively increasing formation of lack of fusion flaws.

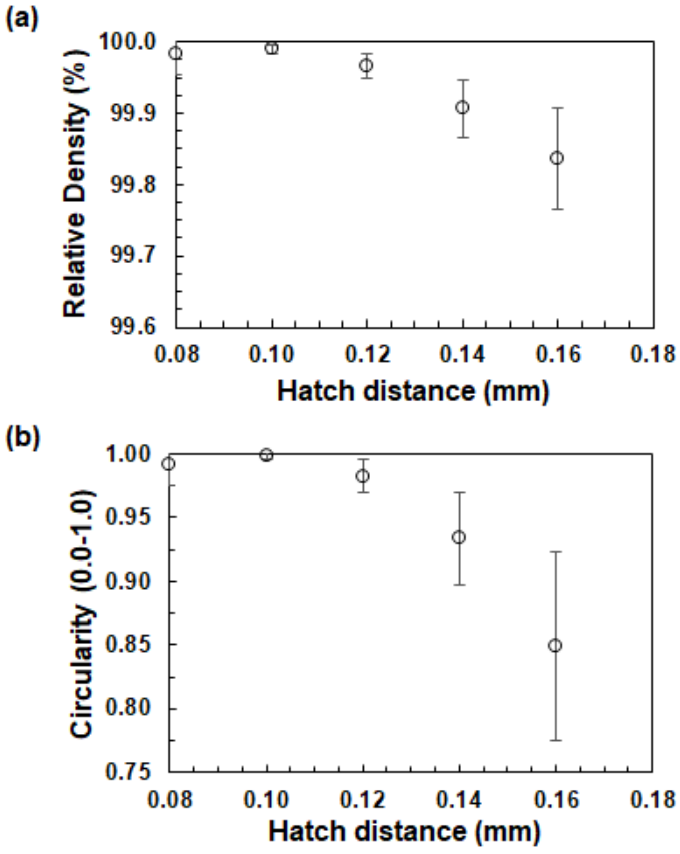

Figure 11: (a) Relative density and (b) flaw circularity as a function of hatch distance with the laser power, scan speed, and slice thickness held constant at 200 W, 800 mm/s, and 0.03 mm, respectively

4.3 Influence of L-PBF parameters on the microstructure

Figure 12 presents characteristic microstructural features of the LPBF-built 316L SS. Parallel to the build direction, a typical melt pool feature was observed as presented in Figure 12(a). Perpendicular to the build direction, discontinuous melt pool tracks were observed as shown in Figure 12(b), due to the scan rotation of 67° employed in this study. Columnar grains orthogonal to the melt pool boundaries within individual melt pools were observed as presented in Figure 12(a). Within the melt pools and within the columnar grains, fine cellular and columnar-cellular structures were observed as presented in Figure 12(c) and Figure 12(d). The difference in aspect ratio observed for these cells would be due to the variation of column orientations observed in 2-dimensional micrographs.

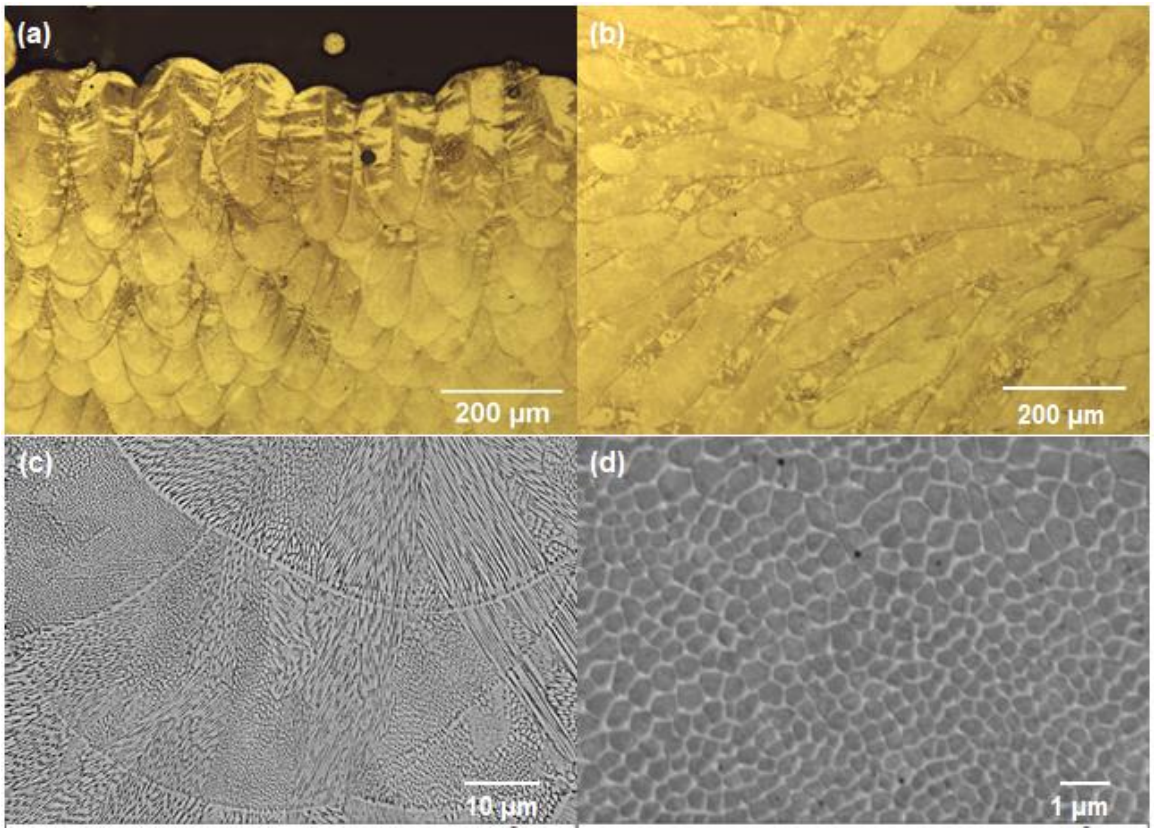

Figure 12: Optical micrographs of the LPBF 316L SS (a) parallel to the build direction and (b) perpendicular to the build direction. Backscattering electron micrographs at (c) low and (d) high magnifications. These samples were produced with a laser power, scan speed, hatch spacing, and slice thickness of 275 W, 1000 mm/s, 0.12 mm, and 0.03 mm, respectively

Melt pool depth and width were measured from the very top layer of the melt pools parallel to the build direction. Figure 13 presents typical melt pools observed from optical microscopy for samples produced as a function of scan speed at laser power of 275 W, hatch spacing of 0.12 mm, and slice thickness of 0.03 mm. These melt pools were only exposed to a single laser scan (i.e., last scan), and symmetry of the melt pool shape was assumed for the measurement. Table 4 presents experimentally measured depth and

width of melt pools in this study. It should be noted that melt pool width and depth could not be determined with confidence when the laser scan speed was exceedingly high, e.g., 3000 mm/s at 275 W and 3000 and 3500 at 350 W, so they are not reported in Table 4.

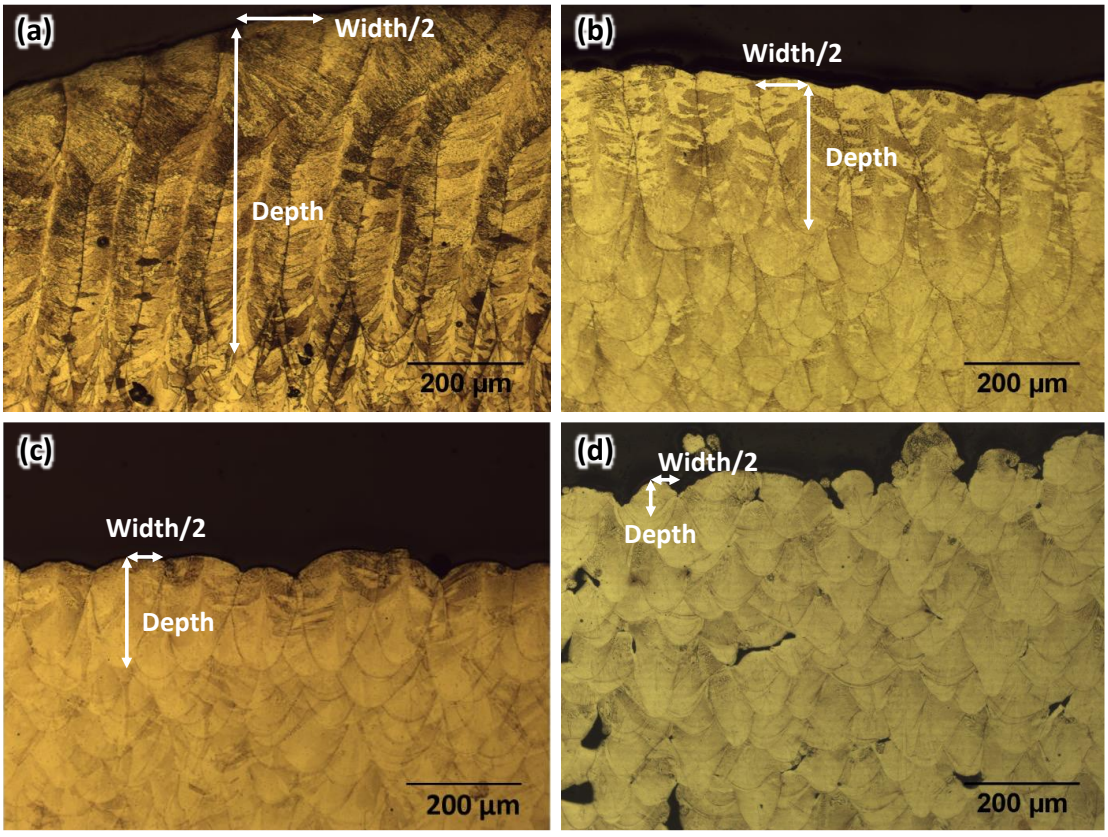

Figure 13: Optical micrographs of melt pools perpendicular to the build direction from the last top layer solidified in 316L SS samples as a function of scan speed: (a) 400 mm/s, (b) 800 mm/s, (c) 1200 mm/s, and (d) 2200 mm/s. Laser power, hatch spacing, and slice thickness were held constant at 275 W, 0.12 mm, and 0.03 mm, respectively

Table 4: Melt pool width and depth determined from experimental measurements

Power (W)	Scan speed (mm/s)	Slice thickness (mm)	Hatch distance (mm)	Volume energy density (J/mm^3)	Melt pool depth exp* (µm)	Melt pool width exp* (µm)
125	100	0.03	0.12	347.22	481 ± 56	254 ± 106
125	200	0.03	0.12	173.61	274 ± 47	210 ± 57
125	400	0.03	0.12	86.81	163 ± 42	151 ± 28
125	600	0.03	0.12	57.87	78 ± 14	120 ± 19
125	800	0.03	0.12	43.40	52 ±12	111 ± 14
200	200	0.03	0.12	277.78	546 ±67	309 ± 77
200	400	0.03	0.12	138.89	368 ± 27	234 ± 35
200	600	0.03	0.12	92.59	268 ± 38	222 ± 41
200	800	0.03	0.12	69.44	169 ± 18	148 ± 19
200	1000	0.03	0.12	55.56	115 ± 25	142 ± 15
200	1200	0.03	0.12	46.30	91 ± 15	114 ± 18
200	1400	0.03	0.12	39.68	62 ± 18	99 ± 22
200	1800	0.03	0.12	30.86	71 ± 30	97 ± 26
200	2200	0.03	0.12	25.25	27 ± 11	63 ± 15
200	2600	0.03	0.12	21.37	52 ± 16	94 ± 22
275	400	0.03	0.12	190.97	590 ± 47	318 ± 140
275	600	0.03	0.12	127.32	394 ± 24	195 ± 29
275	800	0.03	0.12	95.49	290 ± 28	182 ± 31
275	1000	0.03	0.12	76.39	205 ± 27	125 ± 25
275	1200	0.03	0.12	63.66	148 ± 20	130 ± 22
275	1400	0.03	0.12	54.56	98 ± 29	105 ± 18

Power (W)	Scan speed (mm/s)	Slice thickness (mm)	Hatch distance (mm)	Volume energy density (J/mm^3)	Melt pool depth exp* (μm)	Melt pool width exp* (μm)
275	1800	0.03	0.12	42.44	78 ± 25	88 ± 16
275	2200	0.03	0.12	34.72	61 ± 25	68 ± 17
275	2600	0.03	0.12	29.38	53 ± 15	78 ± 19
350	600	0.03	0.12	162.04	605 ± 35	280 ± 125
350	800	0.03	0.12	121.53	409 ± 14	223 ± 57
350	1000	0.03	0.12	97.22	322 ± 30	218 ± 45
350	1200	0.03	0.12	81.02	209 ± 31	138 ± 73
350	1400	0.03	0.12	69.44	152 ± 47	151 ± 39
350	1800	0.03	0.12	54.01	115. ± 34	99 ± 18
350	2200	0.03	0.12	44.19	70 ± 30	87 ± 18
350	2600	0.03	0.12	37.39	81 ± 17	116 ± 21

Note: exp * refers to experimental measurements. These are reported with average _ standard deviation values.

Variation in melt pool width and depth as a function of laser scan speed is presented in Figure 14(a) and Figure 14(b), respectively, for the laser powers employed in this study. Clearly, both the width and depth decrease with an increase in scan speed and a decrease in power. The same result can be plotted as a function of volumetric energy density, as shown in Figure 14(c) and Figure 14(d). Both the width and depth increase with an increase in volumetric energy density up to approximately 200 J/mm^3. However, this trend does not hold, albeit only a few data points, with excessive volumetric energy density above 200 J/mm^3. However, a close examination reveals that the increases in width and depth with volumetric energy density is consistent for a fixed laser power. Therefore, the dispersion in data observed in Figure 14(c) and Figure 14(d) at higher volumetric energy density is a result due to change in laser power (at extremely slow scan speed) that cannot be normalized by volumetric energy density.

The melt pool dimensions examined as functions of LPBF parameters (e.g., power and scan speed) and volumetric energy density also demonstrated that, in terms of absolute scale, the changes in depth were more sensitive than width. For example, the width measured in this study, on average, ranged from 50 to 300 μm, while the depth measured ranged from 30 to 600 μm.

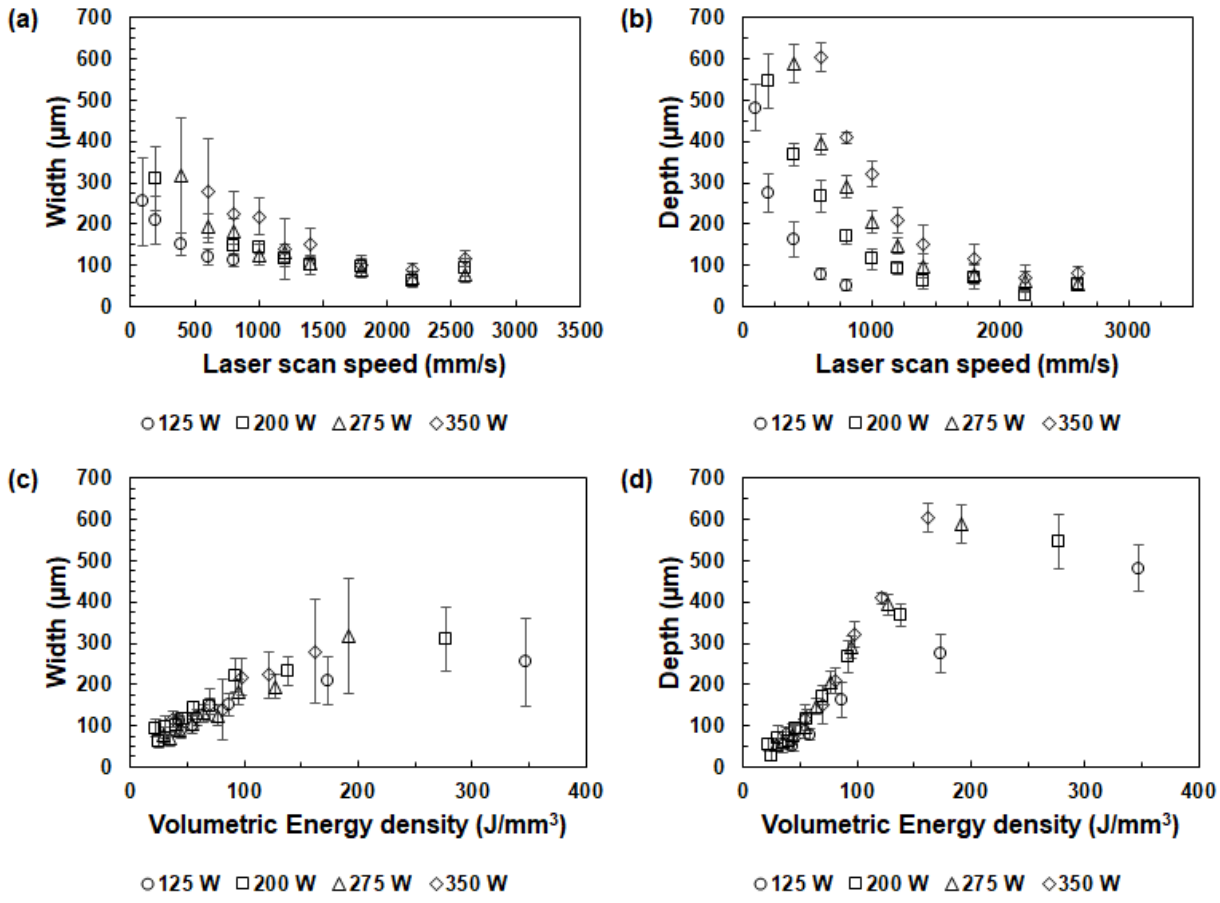

Figure 14: Variation of melt pool (a) width and (b) depth as a function of laser scan speed; and variation of melt pool (c) width and (d) depth as a function of volumetric energy density

Figure 15 shows the calculated criterion defined by Eq. (3) based on experimental measured melt pool dimension as a function of volumetric energy density for the 316L SS samples. A rapid decrease in the value for the criterion of lack-of-fusion is observed when volumetric energy density increased. The volumetric energy density range (highlighted in gray box from 46 J/mm^3 to 127 J/mm^3) that yielded samples with greater than 99.8% relative density closely corresponded to the criterion below 1, except for the lower end, e.g., <55 J/mm^3.

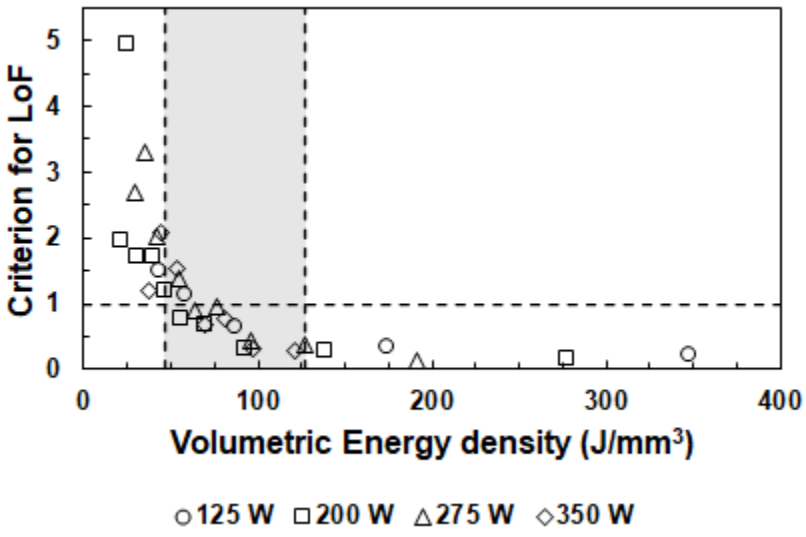

Figure 15: Criterion for lack-of-fusion determined using Equation 3 plotted as a function of energy density. Gray box corresponds to the volumetric energy density that yielded relative density greater than 99.8% [36]

4.4. Summary

This study was designed to investigate the effect of processing parameters on the densification, melt pool morphology and microstructural evolution of LPBF 316L SS using volumetric energy density. Laser power and scan speed were varied over a wide range, systematically and independently.

Key findings of this investigation are:

(1) The energy density input affects the overall pores and flaws observed in LPBF 316L SS. Volumetric energy density, below 46 J/mm^3, yielded lack of fusion flaws due to insufficient melting, while excessive energy density, above 127 J/mm^3, produced keyhole porosity. Between these two extremes, there was a wide range of volumetric energy density in which density greater than 99.8% was achieved.

(2) Width and depth of melt pool increased with higher volumetric energy density (e.g., higher power and slower scan speed).

(3) The threshold for lack of fusion can be used to help identify the onset of optimum LPBF parameters which would yield high density alloy specimens/components.

(4) As-built microstructure in LPBF 316L SS consisted of sub-grain cellular structures within grains observed normal to the boundaries of the melt pool structure.

CHAPTER 5: FLAW TYPE DEPENDENT TENSILE PROPERTIES OF 316L STAINLESS STEEL MANUFACTURED BY LASER POWDER BED FUSION

5.1. Characterization and quantification of flaws

Optical micrographs presented in Figure 16 distinctively present the two types of flaws, observed based on LPBF parameters. At constant power of 200 W, low scan speed, the corresponding high energy input produced KH porosity, typically identified as spherical pores. A nearly full density, ~ 99.9% was observed at the scan speed of 800 mm/s. Then, as the energy input was reduced by increasing the laser scan speed, LoF pores with irregular shape were observed. While the samples produced with scan speed of 200 mm/s and 1,700 mm/s were targeted to have similar relative density, ~94 %, measured density values of 97 % and 91 %, respectively, were observed along with high standard deviation as reported in Table 2 and Figure 16.

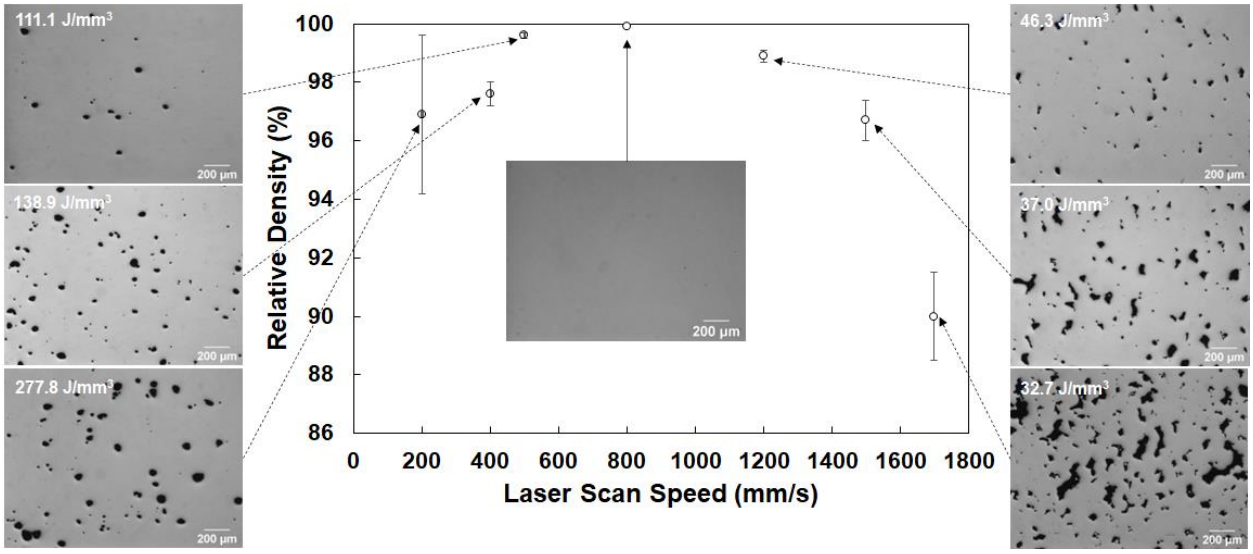

Figure 16: Variation in relative density observed by optical micrographs as a function of laser scan speed in LPBF.

A cursory examination of Figure 16 suggests that the shape and size distribution of the flaws varied as functions of LPBF parameters, i.e., varying scan speed at constant power of 200 W. Figure 17 shows the flaws boxplots for all the samples studied defined by the median, first quartile (Q1), third quartile (Q3), the interquartile range (IQR, likely range of variation), and outliers (surprisingly high maximum and low minimums). The outliers were defined by 1.5 times IQR above the third quartile or 1.5 times IQR below the first quartile [46]. The sample built at 800 mm/s has a negligible number of pores, so its distribution is not shown in the Figure 17.

In general, with an increment of the laser scan speed, the mean circularity for the samples containing majority KH increased. The opposite trend occurred with the samples containing majority LoF as present in Figure 17(a). As shown in the Figure 17(b), the

mean size of the pores was also affected with the processing parameters. The mean Feret diameter of the samples decreased for KH and increased for LoF with a progressive increment of the laser scan speed. More elongated flaws were found when the laser scan speed increased for the LoF pores, but the mean aspect ratio in samples containing KH pores were similar as shown in the Figure 17 (c).

The sample built at 500 mm/s with relative density of 99.6 ± 0.1, exhibited the largest median circularity (0.94) with the narrowest range of circularity distribution (IQR of 0.10), along with the lowest median size (21.99 μm) and median aspect ratio (1.31). The sample built at 1700 mm/s with relative density of 90.0 ± 1.5, had the lowest median circularity (0.67), with the widest range of circularity distribution (IQR of 0.31). Interestingly, this sample build at 1700 mm/s had the same median size as in the sample built at 200 mm/s (34.00 μm), but the largest number of outliers with LoF pores up to 459 μm in size. Even though the samples containing KH pores have some flaws with circularity below 0.6, these were considered outliers since they are believed to be connected pores, located too close to each other given the resolution limit of optical microscopy.

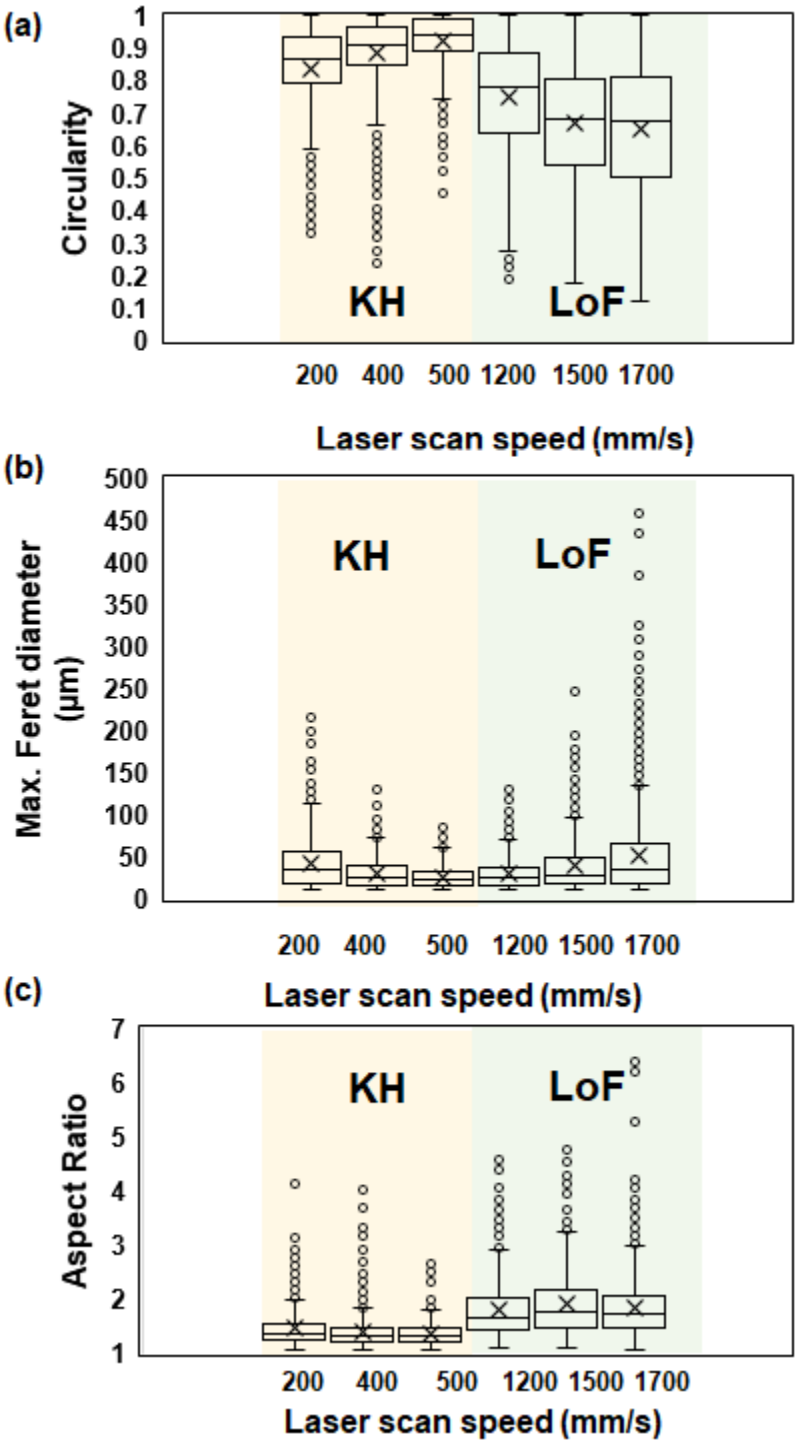

Figure 17: Boxplots for the (a) circularity, (b) Feret diameter, and (c) aspect ratio of the flaws with variation of laser scan speed.

5.2. Mechanical properties

The engineering stress–strain curves for the samples built with targeted density of < 97 %, ~ 98 % and ~ 99 % are presented in Figure 18, and the corresponding mechanical properties determined are reported in Table 2. Although our best effort was to target three levels of density (i.e., > 97 %, ~ 98 % and ~ 99 %) in the KH and LoF domains, some variation in relative density was observed as reported in Table 2. Figure 19 presents yield strength (YS), ultimate tensile strength (UTS) and per cent elongation (%EL) at failure for all the samples as a function of scan speed with the resulting relative density. For samples produced with LPBF parameters containing > 3 %, ~2 %, ~1% flaws, presence of LoF pores yielded lower YS and UTS. The %EL at failure for the samples with relative density < 97 % was lower for those with LoF pores, however, it did not vary significantly for the samples with density of 98 % or higher. Despite the flaw-dependent sensitivity described, the over-arching variable on mechanical properties was the overall density of the 316L SS samples additively manufactured by LPBF.

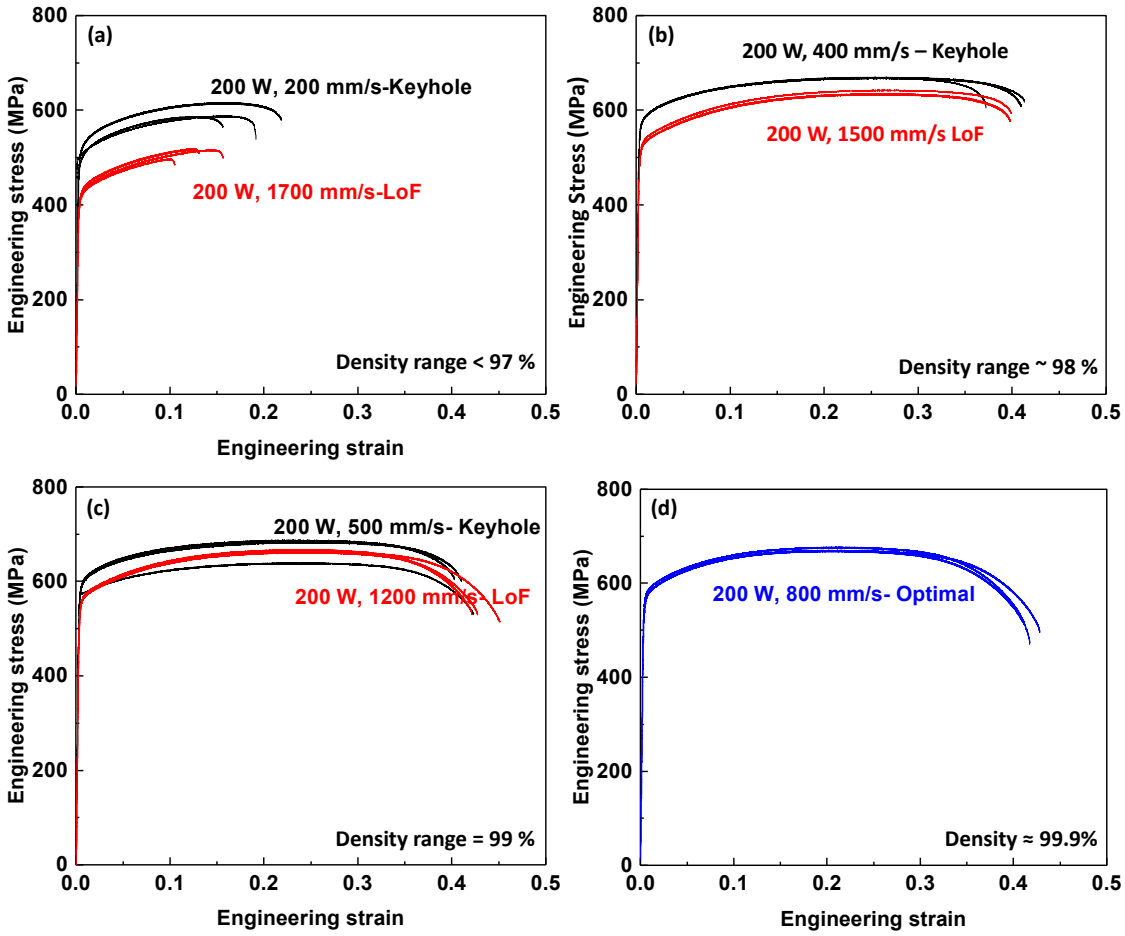

Figure 18: The engineering stress-strain curves acquired in tension from the 316L stainless steel samples built with varying amounts of KH and LoF flaws.

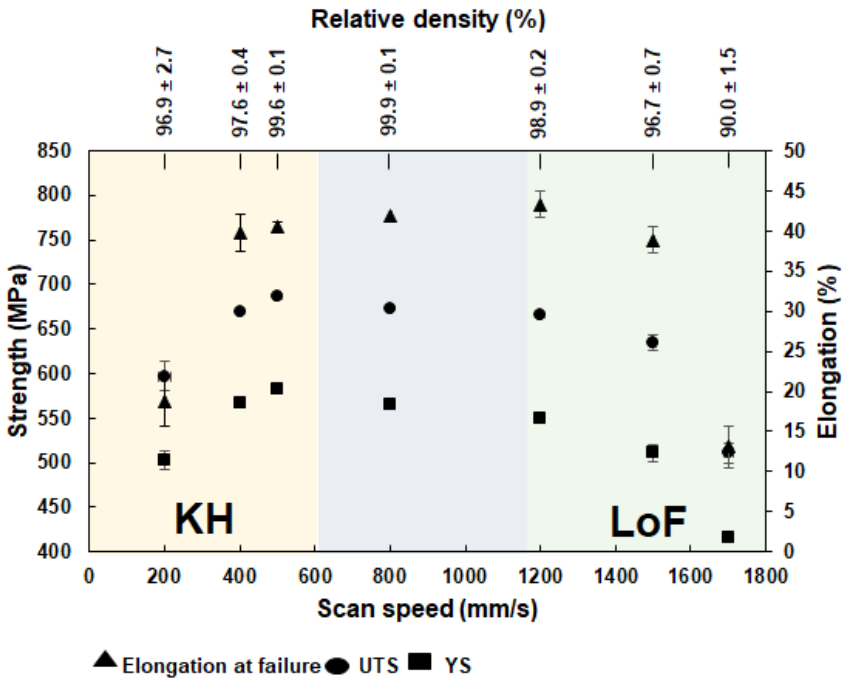

Figure 19: Yield strength (YS), ultimate tensile strength (UTS) and elongation at failure (EL%) as a function of scan speed for the 316L stainless steel samples built with varying amounts of KH and LoF flaws.

5.3. Fracture surface characteristics

Fractured surfaces of tensile specimens were examined using secondary electron micrographs as presented in Figures 20 and Figure 21. At lower magnification, the presence of LoF and KH flaws were very pronounced than those observed by the cross-sectional optical micrographs in Figure 16. This indeed suggests that the fracture path in tension followed preferentially along these flaws. Also, LoF pores produced with higher scan speeds were clearly observed aligned with stripe laser scanning strategy as shown

in Figure 20(a), Figure 20(b) and Figure 20(c). KH pores shown in Figures 20(d), Figure 20(e), and Figure 20(f) were more randomly distributed.

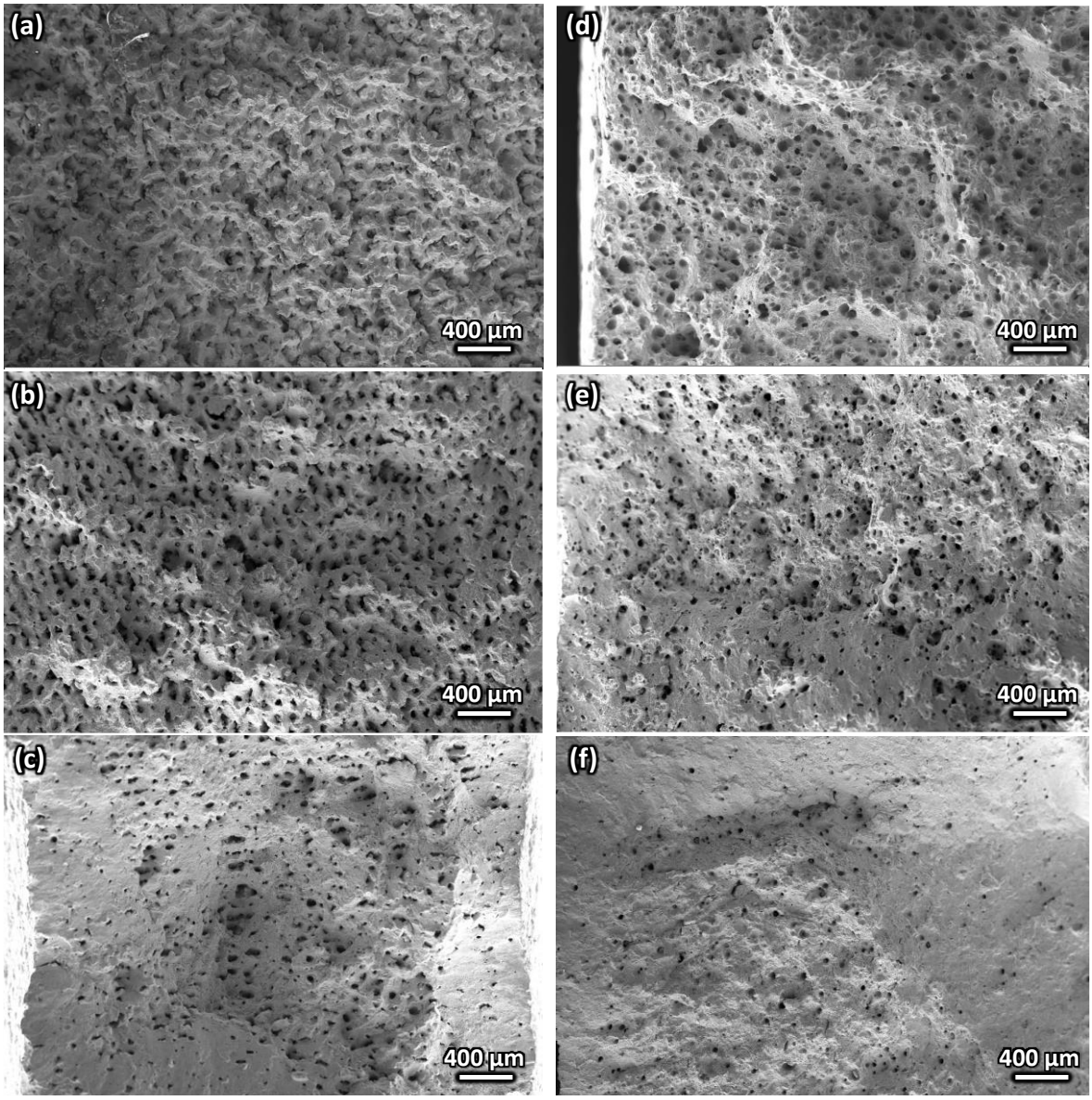

Figure 20: Secondary electron micrographs of fracture surfaces after quasi-static tensile failure experiment. LoF pores were observed in samples produced using laser power and scan speed of (a) 200 W; 1700 mm/s, (b) 200 W; 1500 mm/s and (c) 200 W; 1200 mm/s. KH pores were observed in samples produced using laser power and scan speed of (d) 200 W; 200 mm/s, (e) 200 W; 400 mm/s and (f) 200 W; 500 mm/s.

Irregular shape, high aspect ratio, sharp edges, smooth internal surface, and the presence of un-melted powder particles were the main features of the LoF pores on the fracture surfaces. Many LoF pores contained small spherical particles, presumably unmelted particles, adhered to the interior walls as presented in Figure 21(a). Interconnected of LoF ligaments, either exposed by the fracture (pre-existing internally) or by the crack propagation damage were observed as presented in Figure 21(b).

The KH pores on the fracture surfaces appeared mostly to be isolated, and concentric elliptical rings were found on the interior wall of the KH pores, similar to previous reports [47], [48], as presented in Figure 21(c). Dimples associated with ductile fracture were frequently observed on the fracture surface exposed away from the LoF and KH flaws. The LPBF 316L with nearly full density has high ductility greater than ~40 %EL at failure when it is fully dense [45].

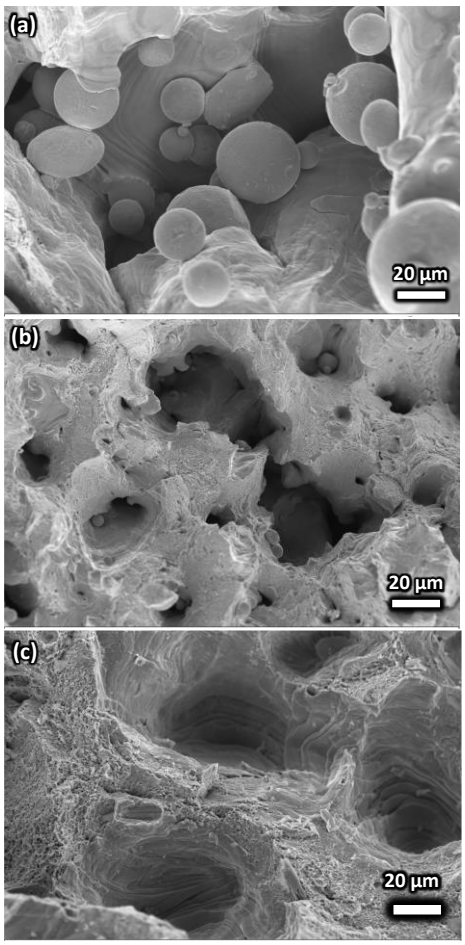

Figure 21: Secondary electron micrographs showing the detailed features of (a,b) LoF pores and (c) KH pores.

5.4. Discussion

According to Figure 19, for the samples built with similar relative density, the ones with a predominant presence of LoF pores exhibited a reduction in strength, but comparable elongation at failure with the samples with KH porosity. Even up to ~2 %

porosity in the KH domain resulted in a similar strength as a sample with negligible porosity. This effect would be due to the more irregular shape of LoF, which can be associated with a higher stress concentration [11], [49]. In addition, LoF pores tend to be larger in size as presented in Figure 19(b).

When the sample built with the fastest scan speed at 1700 mm/s is compared with the other specimens containing LoF pores, built at 1500 mm/s and 1200 mm/s, the average YS for this build condition is approximately 25% and 19% lower, respectively. In addition, there is a significant reduction in average UTS of about ~ 20%, and a notable reduction in %EL at failure. This sample also had the lowest relative density, the largest pores observed, and the most irregular shaped flaws.

The samples built with the lowest scan speed of 200 mm/s, resulting in the lowest relative density among the samples with KH pores, and exhibited approximately 10% reduction in YS, and UTS. The %EL at fracture was reduced in more than 50 % when comparing to the other samples with KH pores. Therefore, the difference in the overall mechanical behavior appeared not to be exclusively, because of the type of flaw present but attributed to the porosity levels.

LPBF 316L SS can exhibit both high strength and elongation despite the presence of flaws. Depending on the processing and testing conditions, the yield strength of the 316L SS LPBF samples vary between 450 and 550 MPa, ultimate tensile strength between 600 and 750 MPa and the ductility between 35 and 55% [50].

5.5. Summary

Laser scan speed was varied to intentionally introduce flaws, namely keyhole and Lack-of-fusion, and the correlation between these types of flaws with tensile properties of LPBF 316L SS was explored. The extreme values of laser scan speed studied (200 mm/s and 1700 mm/s), drove the lower relative density, a decrease in flaw circularity, and increases in size and aspect ratio of the pores in each category. The yield and tensile strength appeared to be more sensitive to the presence of LoF than KH porosity, while the elongation at failure was comparable at low levels of porosity below 2%. However, this sensitivity was not pronounced for LPBF 316L SS due to its high ductility during quasi-static loading.

LIST OF REFERENCES

[1] S. Gorsse, C. Hutchinson, M. Gouné, and R. Banerjee, “Additive manufacturing of metals: a brief review of the characteristic microstructures and properties of steels, Ti-6Al-4V and high-entropy alloys,” *Sci. Technol. Adv. Mater.*, vol. 18, no. 1, pp. 584–610, 2017, doi: 10.1080/14686996.2017.1361305.

[2] T. Debroy *et al.*, “Additive manufacturing of metallic components – Process , structure and properties,” *Prog. Mater. Sci.*, vol. 92, pp. 112–224, 2018, doi: 10.1016/j.pmatsci.2017.10.001.

[3] I. Gibson, D. W. Rosen, and B. Stucker, “Chapter 5 Powder Bed Fusion Processes,” in *Additive Manufacturing Technologies: Rapid Prototyping to Drect Digital Manufacturing*, 2010, pp. 103–142.

[4] R. Li, Y. Shi, Z. Wang, L. Wang, J. Liu, and W. Jiang, “Densification behavior of gas and water atomized 316L stainless steel powder during selective laser melting,” *Appl. Surf. Sci.*, vol. 256, no. 13, pp. 4350–4356, 2010, doi: 10.1016/j.apsusc.2010.02.030.

[5] J. P. Choi *et al.*, “Densification behavior of 316L stainless steel parts fabricated by selective laser melting by variation in laser energy density,” *Mater. Trans.*, vol. 57, no. 11, pp. 1952–1959, 2016, doi: 10.2320/matertrans.M2016284.

[6] T. Larimian, M. Kannan, D. Grzesiak, B. AlMangour, and T. Borkar, “Effect of energy density and scanning strategy on densification, microstructure and mechanical properties of 316L stainless steel processed via selective laser melting,” *Mater. Sci. Eng. A*, vol. 770, no. June 2019, p. 138455, 2020, doi:

10.1016/j.msea.2019.138455.

[7] K. Chadha, Y. Tian, J. G. Spray, and C. Aranas, “Effect of annealing heat treatment on the microstructural evolution and mechanical properties of hot isostatic pressed 316L stainless steel fabricated by laser powder bed fusion,” *Metals (Basel).*, vol. 10, no. 6, pp. 1–18, 2020, doi: 10.3390/met10060753.

[8] International Organization for Standardization, “Standard Terminology for Additive Manufacturing – General Principles – Terminology ISO/ASTM 52900,” pp. 1–9, 2015, [Online]. Available: http://compass.astm.org/EDIT/html_annot.cgi?ISOASTM52900+15.

[9] W. H. Kan *et al.*, “The influence of porosity on Ti-6Al-4V parts fabricated by laser powder bed fusion in the pursuit of process efficiency,” *Int. J. Adv. Manuf. Technol.*, vol. 119, no. 7–8, pp. 5417–5438, 2022, doi: 10.1007/s00170-021-08374-8.

[10] N. Sanaei, A. Fatemi, and N. Phan, “Defect characteristics and analysis of their variability in metal L-PBF additive manufacturing,” *Mater. Des.*, vol. 182, p. 108091, 2019, doi: 10.1016/j.matdes.2019.108091.

[11] T. Montalbano *et al.*, “Uncovering the coupled impact of defect morphology and microstructure on the tensile behavior of Ti-6Al-4V fabricated via laser powder bed fusion,” *J. Mater. Process. Technol.*, vol. 294, no. August 2020, p. 117113, 2021, doi: 10.1016/j.jmatprotec.2021.117113.

[12] R. Fang *et al.*, “Effect of selective laser melting process parameters on the microstructure and properties of a precipitation hardening stainless steel,” *Mater. Des.*, vol. 212, p. 110265, 2021, doi: 10.1016/j.matdes.2021.110265.

[13] A. T. Sutton *et al.*, “Evolution of AISI 304L stainless steel part properties due to

powder recycling in laser powder-bed fusion," *Addit. Manuf.*, vol. 36, no. April, p. 101439, 2020, doi: 10.1016/j.addma.2020.101439.

[14] C. M. Laursen, S. A. DeJong, S. M. Dickens, A. N. Exil, D. F. Susan, and J. D. Carroll, "Relationship between ductility and the porosity of additively manufactured AlSi10Mg," *Mater. Sci. Eng. A*, vol. 795, no. August, p. 139922, 2020, doi: 10.1016/j.msea.2020.139922.

[15] Z. Wu *et al.*, "The effect of defect population on the anisotropic fatigue resistance of AlSi10Mg alloy fabricated by laser powder bed fusion," *Int. J. Fatigue*, vol. 151, no. January, p. 106317, 2021, doi: 10.1016/j.ijfatigue.2021.106317.

[16] L. Zhou *et al.*, "Microstructure and mechanical properties of Zr-modified aluminum alloy 5083 manufactured by laser powder bed fusion," *Addit. Manuf.*, vol. 28, no. March, pp. 485–496, 2019, doi: 10.1016/j.addma.2019.05.027.

[17] D. S. Watring, J. T. Benzing, N. Hrabe, and A. D. Spear, "Effects of laser-energy density and build orientation on the structure–property relationships in as-built Inconel 718 manufactured by laser powder bed fusion," *Addit. Manuf.*, vol. 36, no. June, 2020, doi: 10.1016/j.addma.2020.101425.

[18] H. Hyer *et al.*, "Elimination of extraordinarily high cracking susceptibility of aluminum alloy fabricated by laser powder bed fusion," *J. Mater. Sci. Technol.*, vol. 103, pp. 50–58, 2022, doi: 10.1016/j.jmst.2021.06.023.

[19] J. R. Poulin, A. Kreitcberg, P. Terriault, and V. Brailovski, "Fatigue strength prediction of laser powder bed fusion processed Inconel 625 specimens with intentionally-seeded porosity: Feasibility study," *Int. J. Fatigue*, vol. 132, no. September 2019, 2020, doi: 10.1016/j.ijfatigue.2019.105394.

[20] D. D. Gu, Y. F. Shen, J. L. Yang, and Y. Wang, “Effects of processing parameters on direct laser sintering of multicomponent Cu based metal powder,” *Mater. Sci. Technol.*, vol. 22, no. 12, pp. 1449–1455, 2006, doi: 10.1179/174328406X111057.

[21] A. Sola and A. Nouri, “Microstructural porosity in additive manufacturing: The formation and detection of pores in metal parts fabricated by powder bed fusion,” *J. Adv. Manuf. Process.*, vol. 1, no. 3, pp. 1–21, 2019, doi: 10.1002/amp2.10021.

[22] P. Dhaiveegan, N. Elangovan, T. Nishimura, and N. Rajendran, “Corrosion behavior of 316L and 304 stainless steels exposed to industrial-marine-urban environment: Field study,” *RSC Adv.*, vol. 6, no. 53, pp. 47314–47324, 2016, doi: 10.1039/c6ra04015b.

[23] N. S. Al-Mamun, K. Mairaj Deen, W. Haider, E. Asselin, and I. Shabib, “Corrosion behavior and biocompatibility of additively manufactured 316L stainless steel in a physiological environment: the effect of citrate ions,” *Addit. Manuf.*, vol. 34, no. March, p. 101237, 2020, doi: 10.1016/j.addma.2020.101237.

[24] D. Kong *et al.*, “Heat treatment effect on the microstructure and corrosion behavior of 316L stainless steel fabricated by selective laser melting for proton exchange membrane fuel cells,” *Electrochim. Acta*, vol. 276, pp. 293–303, 2018, doi: 10.1016/j.electacta.2018.04.188.

[25] J. P. Oliveira, T. G. Santos, and R. M. Miranda, “Revisiting fundamental welding concepts to improve additive manufacturing: From theory to practice,” *Prog. Mater. Sci.*, vol. 107, no. August 2019, p. 100590, 2020, doi: 10.1016/j.pmatsci.2019.100590.

[26] C. Tenbrock *et al.*, “Influence of keyhole and conduction mode melting for top-hat

shaped beam profiles in laser powder bed fusion," *J. Mater. Process. Technol.*, vol. 278, no. May 2019, p. 116514, 2020, doi: 10.1016/j.jmatprotec.2019.116514.

[27] J. Trapp, A. M. Rubenchik, G. Guss, and M. J. Matthews, "In situ absorptivity measurements of metallic powders during laser powder-bed fusion additive manufacturing," *Appl. Mater. Today*, vol. 9, pp. 341–349, 2017, doi: 10.1016/j.apmt.2017.08.006.

[28] Y. Huang *et al.*, "Keyhole fluctuation and pore formation mechanisms during laser powder bed fusion additive manufacturing," *Nat. Commun.*, vol. 13, no. 1, pp. 1–11, 2022, doi: 10.1038/s41467-022-28694-x.

[29] Y. M. Wang *et al.*, "Additively manufactured hierarchical stainless steels with high strength and ductility," *Nat. Mater.*, vol. 17, no. 1, pp. 63–70, 2018, doi: 10.1038/NMAT5021.

[30] D. Herzog, V. Seyda, E. Wycisk, and C. Emmelmann, "Additive manufacturing of metals," *Acta Mater.*, vol. 117, pp. 371–392, 2016, doi: 10.1016/j.actamat.2016.07.019.

[31] J. Suryawanshi, K. G. Prashanth, and U. Ramamurty, "Mechanical behavior of selective laser melted 316L stainless steel," *Mater. Sci. Eng. A*, vol. 696, no. January, pp. 113–121, 2017, doi: 10.1016/j.msea.2017.04.058.

[32] Y. Zhong, L. Liu, S. Wikman, D. Cui, and Z. Shen, "Intragranular cellular segregation network structure strengthening 316L stainless steel prepared by selective laser melting," *J. Nucl. Mater.*, vol. 470, pp. 170–178, 2016, doi: 10.1016/j.jnucmat.2015.12.034.

[33] M. C. Brennan, J. S. Keist, and T. A. Palmer, "Defects in Metal Additive

Manufacturing Processes," *J. Mater. Eng. Perform.*, vol. 30, no. 7, pp. 4808–4818, 2021, doi: 10.1007/s11665-021-05919-6.

[34] J. P. Oliveira, A. D. LaLonde, and J. Ma, "Processing parameters in laser powder bed fusion metal additive manufacturing," *Mater. Des.*, vol. 193, pp. 1–12, 2020, doi: 10.1016/j.matdes.2020.108762.

[35] T. Mukherjee, J. S. Zuback, A. De, and T. DebRoy, "Printability of alloys for additive manufacturing," *Sci. Rep.*, vol. 6, pp. 1–8, 2016, doi: 10.1038/srep19717.

[36] M. Tang, P. C. Pistorius, and J. L. Beuth, "Prediction of lack-of-fusion porosity for powder bed fusion," *Addit. Manuf.*, vol. 14, pp. 39–48, 2017, doi: 10.1016/j.addma.2016.12.001.

[37] M. Laleh *et al.*, "A critical insight into lack-of-fusion pore structures in additively manufactured stainless steel," *Addit. Manuf.*, vol. 38, p. 101762, 2021, doi: 10.1016/j.addma.2020.101762.

[38] M. R. Kabir and H. Richter, "Modeling of processing-induced pore morphology in an additively-manufactured Ti-6Al-4V alloy," *Materials (Basel).*, vol. 10, no. 2, 2017, doi: 10.3390/ma10020145.

[39] A. E. Wilson-Heid, T. C. Novak, and A. M. Beese, "Characterization of the Effects of Internal Pores on Tensile Properties of Additively Manufactured Austenitic Stainless Steel 316L," *Exp. Mech.*, vol. 59, no. 6, pp. 793–804, 2019, doi: 10.1007/s11340-018-00465-0.

[40] L. X. Meng *et al.*, "Effects of embedded spherical pore on the tensile properties of a selective laser melted Ti6Al4V alloy," *Mater. Sci. Eng. A*, vol. 815, no. April, 2021, doi: 10.1016/j.msea.2021.141254.

[41] F. H. Kim, S. P. Moylan, T. Q. Phan, and E. J. Garboczi, “Investigation of the Effect of Artificial Internal Defects on the Tensile Behavior of Laser Powder Bed Fusion 17–4 Stainless Steel Samples: Simultaneous Tensile Testing and X-Ray Computed Tomography,” *Exp. Mech.*, vol. 60, no. 7, pp. 987–1004, 2020, doi: 10.1007/s11340-020-00604-6.

[42] A. du Plessis, I. Yadroitsava, and I. Yadroitsev, “Effects of defects on mechanical properties in metal additive manufacturing: A review focusing on X-ray tomography insights,” *Mater. Des.*, vol. 187, p. 108385, 2020, doi: 10.1016/j.matdes.2019.108385.

[43] H. D. Carlton, A. Haboub, G. F. Gallegos, D. Y. Parkinson, and A. A. MacDowell, “Damage evolution and failure mechanisms in additively manufactured stainless steel,” *Mater. Sci. Eng. A*, vol. 651, pp. 406–414, 2016, doi: 10.1016/j.msea.2015.10.073.

[44] C. A. Schneider, W. S. Rasband, and K. W. Eliceiri, “NIH Image to ImageJ: 25 years of image analysis,” *Nat. Methods*, vol. 9, no. 7, pp. 671–675, 2012, doi: 10.1038/nmeth.2089.

[45] N. D. Vallejo, C. Lucas, N. Ayers, K. Graydon, H. Hyer, and Y. Sohn, “Process optimization and microstructure analysis to understand laser powder bed fusion of 316l stainless steel,” *Metals (Basel).*, vol. 11, no. 5, 2021, doi: 10.3390/met11050832.

[46] J. W. Tukey, *Exploratory data analysis*, vol. 2. Reading, MA, 1977.

[47] J. L. Zou, S. K. Wu, W. X. Yang, Y. He, and R. S. Xiao, “A novel method for observing the micro-morphology of keyhole wall during high-power fiber laser

welding,” *Mater. Des.*, vol. 89, pp. 785–790, 2016, doi: 10.1016/j.matdes.2015.10.039.

[48] G. Kasperovich, J. Haubrich, J. Gussone, and G. Requena, “Correlation between porosity and processing parameters in TiAl6V4 produced by selective laser melting,” *Mater. Des.*, vol. 105, pp. 160–170, 2016, doi: 10.1016/j.matdes.2016.05.070.

[49] C. Qiu, H. Chen, Q. Liu, S. Yue, and H. Wang, “On the solidification behaviour and cracking origin of a nickel-based superalloy during selective laser melting,” *Mater. Charact.*, vol. 148, no. December 2018, pp. 330–344, 2019, doi: 10.1016/j.matchar.2018.12.032.

[50] K. G. Prashanth and J. Eckert, “Formation of metastable cellular microstructures in selective laser melted alloys,” *J. Alloys Compd.*, vol. 707, pp. 27–34, 2017, doi: 10.1016/j.jallcom.2016.12.209.